

Dark matter annihilation to neutrinos

Carlos A. Argüelles^{ID*}

*Department of Physics and Laboratory for Particle Physics and Cosmology,
Harvard University, Cambridge, Massachusetts 02138, USA*

Alejandro Diaz[†]

*Department of Physics, Massachusetts Institute of Technology,
Cambridge, Massachusetts 02139, USA*

Ali Kheirandish[‡]

*Department of Physics and Center for Multimessenger Astrophysics,
Institute for Gravitation and the Cosmos, The Pennsylvania State University,
University Park, Pennsylvania 16802, USA*

Andrés Olivares-Del-Campo[§]


*Institute for Particle Physics Phenomenology (IPPP), Durham University,
Durham DH1 3LE, United Kingdom*

Ibrahim Safa^{||}

*Department of Physics and Wisconsin IceCube Particle Astrophysics Center,
University of Wisconsin, Madison, Wisconsin 53706, USA
and Department of Physics and Laboratory for Particle Physics and Cosmology,
Harvard University, Cambridge, Massachusetts 02138, USA*

Aaron C. Vincent[¶]

*Department of Physics, Engineering Physics and Astronomy, Queen's University,
Kingston, Ontario K7L 3N6, Canada,
Arthur B. McDonald Canadian Astroparticle Physics Research Institute, Kingston,
Ontario K7L 3N6, Canada,
and Perimeter Institute for Theoretical Physics, Waterloo, Ontario N2L 2Y5, Canada*

 (published 16 September 2021)

The annihilation of dark matter into neutrinos over a range of dark matter masses from MeV/c^2 to ZeV/c^2 is reviewed. Thermally produced models of dark matter are expected to self-annihilate to standard model products. As no such signal has yet been detected, neutrino detectors are turned to in order to constrain the “most invisible channel.” The experimental techniques that are used to detect neutrinos are reviewed, and the expected contributions to the neutrino flux at current and upcoming neutrino experiments is revisited. Updated constraints are placed on the dark matter self-annihilation cross section to neutrinos $\langle\sigma v\rangle$ using the most recent data, and the sensitivity of upcoming experiments such as Hyper-Kamiokande, Deep Underground Neutrino Experiment (DUNE), and IceCube Gen2 is forecasted. Where possible, limits and projections are scaled to a single set of dark matter halo parameters for consistent comparison. Galactic and extragalactic signals of s -, p -, and d -wave annihilation processes directly into neutrino pairs are considered, yielding constraints that range from $\langle\sigma v\rangle \sim 2.5 \times 10^{-26} \text{ cm}^3 \text{ s}^{-1}$ at $30 \text{ MeV}/c^2$ to $10^{-17} \text{ cm}^3 \text{ s}^{-1}$ at $10^{11} \text{ GeV}/c^2$. Experiments that report directional and energy information of their events provide much stronger constraints, outlining the importance of making such data public.

DOI: [10.1103/RevModPhys.93.035007](https://doi.org/10.1103/RevModPhys.93.035007)

*carguelles@fas.harvard.edu

†diaza@mit.edu

‡kheirandish@psu.edu

§andres181192@gmail.com

||isafa@fas.harvard.edu

¶aaron.vincent@queensu.ca

CONTENTS

I. Introduction	2
II. Dark Matter Annihilation	3
A. Galactic contribution	4
B. Extragalactic contribution	5
C. Velocity-dependent annihilation	6

III. Experimental Methods	7
A. Statistical methods	8
1. Background-agnostic methods	8
2. Background-informed methods	8
B. Neutrino detection methods	9
1. Neutrino energies below 10 MeV	9
2. Neutrino energies between 10 MeV and 1 GeV	9
3. Neutrino energies from 1 to 10^7 GeV	10
4. Neutrino energies above 10^7 GeV	11
IV. Results	12
A. Velocity-dependent annihilation	20
B. Dark matter halo uncertainties	20
V. Discussion and Conclusions	21
Acknowledgments	22
References	23

I. INTRODUCTION

The standard model (SM) of particle physics is the framework that describes matter and its interactions at the most fundamental level. Despite overwhelming success as a predictive theory, observations indicate that the SM is incomplete. Neutrinos have nonzero masses, yet the Higgs mechanism that provides masses for the other SM fermions cannot account for the chiral nature of neutrinos and their interactions unless additional particle content is added to the model. Additionally, overwhelming astrophysical and cosmological evidence points to the existence of a new species of weakly interacting particles, dark matter (DM), which accounts for $\sim 85\%$ of the mass budget of the Universe. Local stellar dynamics, galactic rotation curves (Rubin, Ford, and Kent, 1970; Persic, Salucci, and Stel, 1996), cluster dynamics (Smith, 1936; Zwicky, 1937), and gravitational lensing (Jee *et al.*, 2007; Jee and Tyson, 2009) all point to mass-to-light ratios in astrophysical objects that are much higher than could be accounted for by stellar objects and gas; for a historical overview see Bertone and Hooper (2018). Measured primordial abundances of light elements tell us that big bang nucleosynthesis requires a total baryon density¹ of only $\Omega_b \sim 0.05$, while the cosmic microwave background (CMB) and other probes of large-scale structures require the total density of nonrelativistic matter to be $\Omega_m \sim 0.3$.²

A leading hypothesis for the nature of this new nonbaryonic component is the weakly interacting massive particle (WIMP). The relic abundance of WIMPs today was set as they fell out of equilibrium with the high-temperature plasma of the early Universe. When the temperature T fell below the DM mass m_χ ,³ the equilibrium distribution became Boltzmann suppressed, namely, $\sim \exp(-m_\chi/T)$. At some point, the expansion rate $H(t)$ became larger than the thermally averaged

self-annihilation rate, preventing further annihilation into SM particles and freezing out the relative density of the DM particles. The WIMP scenario predicts the observed relic abundance of DM for values of the thermally averaged self-annihilation rate $\langle \sigma v \rangle \simeq 3 \times 10^{-26} \text{ cm}^3 \text{ s}^{-1}$ regardless of the final annihilation channel.

Thermal production of weakly interacting DM in the early Universe implies possible ongoing self-annihilation to SM particles wherever DM exists today. Significant effort has gone into searches for indirect signatures of DM annihilation. Annihilation to most SM states yields an abundance of photons with energies of the order of 10% of the DM mass, such that some of the strongest constraints on particle DM models are from the (non)observation of x- and gamma-ray signals from the Milky Way and its satellite galaxies; see Albert *et al.* (2017b) and Hoof, Geringer-Sameth, and Trotta (2018). Cosmic-ray signatures provide similarly constraining limits, reports of excesses notwithstanding; see Boudaud *et al.* (2020) and references therein.

As x- and gamma-ray experiments rely, by design, on electromagnetic signals, they are optimal for probing links between the dark sector and quarks or charged leptons, although neutrino detectors can still play a role in these searches (Cappiello and Beacom, 2019). There is a distinct possibility, however, that the principal portal through which the DM interacts with the SM is via the neutrino sector (Blennow *et al.*, 2019). This naturally arises in “scotogenic” models, in which neutrino mass generation occurs through interactions with the dark sector (Boehm *et al.*, 2008; Farzan and Ma, 2012; Escudero, Rius, and Sanz, 2017a, 2017b; Hagedorn *et al.*, 2018; Alvey and Fairbairn, 2019; Baumholzer *et al.*, 2019; Patel, Profumo, and Shakya, 2019). These models introduce heavy neutrino states, sometimes called dark neutrinos, which could also provide a possible explanation for the MiniBooNE anomaly (Bertuzzo *et al.*, 2018; Ballett, Hostert, and Pascoli, 2019a, 2019b; Ballett, Pascoli, and Ross-Lonergan, 2019). “Secret” neutrino interactions with dark matter have recently become an active field of investigation, where constraints have been obtained using high-energy astrophysical neutrinos (Farzan and Palomares-Ruiz, 2014, 2019; Davis and Silk, 2015; Cherry, Friedland, and Shoemaker, 2016; Argüelles, Kheirandish, and Vincent, 2017; Capozzi, Shoemaker, and Vecchi, 2018; Kelly and Machado, 2018; Choi, Kim, and Rott, 2019; Murase and Shoemaker, 2019; Pandey, Karmakar, and Rakshit, 2019), solar neutrinos (Capozzi, Shoemaker, and Vecchi, 2017), cosmology (Olivares-Del Campo *et al.*, 2018; Barenboim, Denton, and Oldengott, 2019), accelerator neutrino experiments (Aguilar-Arevalo *et al.*, 2017; Argüelles, Hostert, and Tsai, 2018; Hostert, 2019), and colliders (Primulando and Uttayarat, 2018).

Neutrinos are light, neutral, and difficult to detect. If DM annihilates to heavy states such as muons, quarks, or weak bosons, a neutrino signal will be produced. Unless annihilation occurs in an optically thick environment, the associated photon signal will always be easier to detect. We thus focus on the most invisible channel: direct annihilation of DM into neutrino-antineutrino pairs, whose energy will be equal to the DM rest mass, i.e., $E_\nu = m_\chi$.

¹By “baryonic” we refer here to stable nonrelativistic matter made of SM particles including neutrons, protons, and electrons.

²More precisely, the baryon density is inferred as $\Omega_b h^2 = 0.0224 \pm 0.0001$ and the cold DM density is $\Omega_c h^2 = 0.120 \pm 0.001$ (Aghanim *et al.*, 2018), where Ω_i is the ratio of the density of the component i to the critical density and the Hubble constant is $H_0 \equiv h 100 \text{ km s}^{-1} \text{ Mpc}^{-1}$.

³We work in natural units where $c = \hbar = k_B = 1$.

In the past two decades we have seen extraordinary progress in the field of neutrino physics. Observations span a wide energy range, from the MeV pp solar neutrino flux (Agostini *et al.*, 2018) to the PeV (10^6 GeV) high-energy astrophysical neutrinos (Aartsen *et al.*, 2013, 2014c; Schneider, 2019). Furthermore, limits exist all the way up to \sim ZeV (10^{12} GeV) (Aab *et al.*, 2015a; Aartsen *et al.*, 2018). With these observations, a multitude of experimental constraints have been derived on the DM annihilation cross section to neutrino pairs, either by experimental collaborations themselves or by independent researchers recasting results of previous searches. The goal of this review is to collect, when available, existing constraints on the $\chi\chi \rightarrow \nu\bar{\nu}$ annihilation channel, and otherwise to compute such limits from the available data. We focus on the two most promising sources of DM annihilation signals: (1) the dark matter halo of the Milky Way, in which we are deeply embedded, and (2) the full cosmic flux from the sum of all DM halos within our cosmological horizon.

Our main results are a set of constraints on a constant (s -wave) thermally averaged annihilation cross section $\langle\sigma v\rangle$. Where possible, we also compute constraints on p -wave [$\langle\sigma v\rangle \propto (v/c)^2$] and d -wave [$\langle\sigma v\rangle \propto (v/c)^4$] suppressed annihilations. These results are provided in Figs. 2–6. We cover a mass range from 1 to 10^{15} MeV. While the upper limit is a function of the experimental reach, neutrino-coupled dark matter is severely constrained below ~ 10 MeV based on its modification of N_{eff} , the energy density in relativistic particles during nucleosynthesis (Kolb, Turner, and Walker, 1986; Serpico and Raffelt, 2004; Boehm, Dolan, and McCabe, 2012; Boehm, Dolan, and McCabe, 2013; Ho and Scherrer, 2013; Steigman, 2013; Nollett and Steigman, 2014, 2015; Steigman and Nollett, 2014; Wilkinson *et al.*, 2016; Escudero, 2019; Sabti *et al.*, 2020).

The neutrino flux from DM annihilation sensitively depends on the DM halo shape, and many different assumptions have been employed, some in contradiction to kinematic observations (Benito, Cuoco, and Iocco, 2019). We thus embark on the endeavor to rescale or recompute all constraints using a single set of DM halo parameters. Depending on the nature of the study and the available data, this is not always possible; when this is the case we explicitly mention it. We provide in Sec. V estimates on the uncertainties associated with the choice of DM halo parameters.

This review contains the most up-to-date constraints. While a few experiments have come close in certain narrow mass ranges, current observations are not yet able to probe annihilation cross sections that explain the observed relic abundance of DM through thermal freeze-out. This leaves plenty of room for future searches, which is why we also present a forecast of possible limits from upcoming neutrino experiments (Argüelles *et al.*, 2019).

The structure of this review is as follows: We begin in Sec. II with a review of the annihilation signal we are constraining, from the Milky Way halo in Sec. II.A and from the isotropic background of extragalactic halos in Sec. II.B. In Sec. II.C we detail the calculations needed to extend our analysis to velocity-dependent annihilations, namely, p -wave and d -wave processes. Section III summarizes the

experimental techniques used for neutrino detection in a wide energy range and describes the statistical methods employed in this review to constrain the neutrino flux from dark matter annihilation. Our results are presented in Sec. IV, including results from previous analyses that we recast to be consistent with our halo assumptions wherever possible. Section IV.B shows the results of varying these assumptions in the range allowed by stellar dynamic observations for the galactic component and simulation results for the extragalactic one. Finally, we conclude in Sec. V.

II. DARK MATTER ANNIHILATION

Neutrinos are the most weakly interacting stable particles in the SM and, consequently, the hardest to detect. In the context of indirect detection, this implies that models where DM annihilates predominantly to neutrinos are difficult to rule out. This makes the study of neutrinos as a final-state particle particularly interesting, as all direct and indirect searches for the footprints of DM-SM interactions to date have been unsuccessful (Arcadi *et al.*, 2018; Tanabashi *et al.*, 2018). The limits derived on the DM annihilation to neutrinos can be interpreted as an upper bound on the total DM annihilation cross section to SM particles (Beacom, Bell, and Mack, 2007; Yüksel *et al.*, 2007) since the latter is larger by definition.

From a particle physics point of view, the direct annihilation of DM to neutrinos at tree level requires the addition of a neutrino-DM term to the SM Lagrangian that couples them. Since neutrinos belong to an SU(2) doublet, naive SM gauge invariance implies that coupling neutrinos with DM would also induce an interaction between the DM and the charged leptons, mediated, e.g., by a new Z-like particle. Such interactions are highly constrained, as they lead to the production of dijet or dilepton signatures observable at colliders [see Carena *et al.* (2004) and Lees *et al.* (2014)], fixed target experiments (Abrahamyan *et al.*, 2011), and direct detection experiments [see Blanco *et al.* (2019) and references therein].

Nevertheless, there are viable models in which the DM phenomenology is dominated by its interactions with neutrinos (Blennow *et al.*, 2019). Coupling only to the heavier lepton generations can strongly mitigate bounds from electron interactions by introducing a $U(1)_{L_\mu-L_\tau}$ symmetry (He *et al.*, 1991a, 1991b). A more elegant option allows the DM to interact with a sterile neutrino that then mixes with the active neutrinos, leading to direct annihilations of DM to neutrinos if the mass of the sterile neutrino is larger than the DM mass (Profumo *et al.*, 2018; Ballett, Hostert, and Pascoli, 2019a). If the sterile-light mixing is sizable, DM-neutrino interactions will provide the best window to understand such DM models. A comprehensive review of these scenarios was given by Blennow *et al.* (2019).

Finally, we are considering direct annihilation to neutrinos without including electroweak (EW) corrections, which severely complicate the spectral shape computations. These are important at energies above the electroweak scale and have two main consequences: (1) the peak of the spectrum will be slightly broadened, and (2) a lower-energy continuum will be produced. Given the typical energy resolution ($\gtrsim 10\%$) (Aartsen *et al.*, 2014a) for high-energy neutrino detectors,

the former effect is not likely to be important. The latter effect could potentially lead to stronger bounds from the additional flux at lower energies. A detailed computation of this effect up to ultrahigh energies was only recently performed (Bauer, Rodd, and Webber, 2020); as these calculations were not available at the time of this analysis we do not include them here. At sub-TeV energies, these corrections are accurately implemented in numerical codes such as PYTHIA (Sjöstrand *et al.*, 2015; Sjöstrand, 2020); a comparison between our limits and the ones derived using these additional corrections show little difference; see Liu *et al.* (2020).

A more important consequence is the presence of gamma radiation from the decay of EW products, which can potentially provide complementary constraints to dedicated neutrino-line searches (Murase and Beacom, 2012). Using these secondary products, current constraints on the thermally averaged annihilation cross section to neutrinos from Fermi-LAT and HESS hover around $10^{-23} \text{ cm}^3 \text{ s}^{-1}$ in the 300 GeV to 3 TeV mass range (Queiroz, Yaguna, and Weniger, 2016). These gamma-ray-based constraints are at the same level as current bounds from ANTARES (Adrian-Martinez *et al.*, 2015) but are expected to be improved using next-generation gamma-ray experiments such as the Cherenkov Telescope Array (CTA) (Queiroz, Yaguna, and Weniger, 2016). We provide an example using these projections for CTA in Sec. IV, noting that this includes prompt gamma rays only. Inverse-Compton scattering of primary electrons and positrons with interstellar photons will strengthen the sensitivity of gamma-ray searches. This effect has been studied for DM decay searches, but not for annihilation $\chi\chi \rightarrow \nu\bar{\nu}$ (Murase *et al.*, 2015; Cohen *et al.*, 2017; Chianese *et al.*, 2019).

A. Galactic contribution

We begin by setting limits on DM annihilation to neutrino pairs in the Milky Way (MW) dark matter halo. The expected flux per flavor of neutrinos plus antineutrinos at Earth, assuming equal flavor composition,⁴ is given by

$$\frac{d\Phi_{\nu+\bar{\nu}}}{dE_\nu} = \frac{1}{4\pi} \frac{\langle\sigma v\rangle}{\kappa} \frac{1}{3} \frac{dN_\nu}{dE_\nu} J(\Omega), \quad (1)$$

where κ is 2 for Majorana DM and 4 for Dirac DM, m_χ is the DM mass, and $\langle\sigma v\rangle$ is the thermally averaged self-annihilation cross section into all neutrino flavors. Going forward we set $\kappa = 2$ (Majorana DM). The spectrum in the case of annihilation to two neutrinos is simply $dN_\nu/dE_\nu = 2\delta(1 - E/m_\chi)m_\chi/E^2$. $J(\Omega)$ is a three-dimensional integral over the target solid angle in the sky $d\Omega$ and the distance dx along the line of sight (LOS) of the DM density ρ_χ , namely,

$$J \equiv \int d\Omega \int_{\text{LOS}} \rho_\chi^2(x) dx. \quad (2)$$

It is referred to as the J factor and has units of $\text{GeV}^2 \text{ cm}^{-5} \text{ sr}^5$. The galactocentric distance is

$$r = \sqrt{R_0^2 - 2xR_0 \cos\psi + x^2}, \quad (3)$$

where ψ is the angle between the Galactic Center (GC) and the line of sight and R_0 is the distance from the Sun to the GC. In practice, the upper limit of integration can be set at

$$x_{\text{max}} = \sqrt{R_{\text{halo}}^2 - \sin^2\psi R_0^2 + R_0 \cos\psi}, \quad (4)$$

for some maximum halo radius R_{halo} . The J factor remains approximately unchanged for $R_{\text{halo}} \gtrsim 30$ kpc.

To parametrize the DM halo, we use a generalized Navarro-Frenk-White (NFW) profile, which is given by

$$\rho_\chi(r) = \rho_s \frac{2^{3-\gamma}}{(r/r_s)^\gamma (1 + r/r_s)^{3-\gamma}}. \quad (5)$$

We take the Sun to be located $R_0 = 8.127$ kpc from the GC, as determined by recent measurements of the four-telescope interferometric beam-combiner instrument GRAVITY (Abuter *et al.*, 2018). We use DM halo parameters compatible with the best-fit values of Benito, Cuoco, and Iocco (2019), i.e., a local density⁶ of $\rho_0 = 0.4 \text{ GeV cm}^{-3}$, a slope parameter $\gamma = 1.2$, and a density ρ_s at scale radius $r_s = 20$ kpc. The resulting J factors for s -, p -, and d -wave annihilation are shown in Table I; the last cases will be discussed in Sec. II.C. Some experiments, such as the Antarctic Impulsive Transient Antenna (ANITA), AUGER, and the Giant Radio Array for Neutrino Detection (GRAND), are sensitive only to a certain region of the sky. In these cases, the corresponding J factors must be recomputed by converting their respective sensitivity from elevation and azimuth to galactic coordinates and integrating over the resulting region. A value of the J factor is not given for some experiments, where the flux cannot be factored out as in Eq. (1). This could be due to an energy-dependent acceptance. These values are also shown in Table I. When the exposure is not a simple declination window, we provide the reference from which it can be obtained. Recent works (Benito *et al.*, 2017; Benito, Cuoco, and Iocco, 2019; Karukes *et al.*, 2019; Pato, Iocco, and Bertone, 2015) have constrained the halo shape and density parameters using observations of stellar dynamics in the MW. In Sec. IV.B, we illustrate the effect on the dark matter limits obtained in this review when varying the parameters within those constraints.

⁴If the flavor composition at the source is not democratic, neutrino oscillation will yield a flavor composition at Earth that is close, but not equal to, $(\nu_e:\nu_\mu:\nu_\tau) = (1:1:1)$. Annihilation to only ν_e will give $\sim(0.55:0.25:0.2)$; annihilation to ν_μ gives $\sim(0.25:0.36:0.38)$ and ν_τ yields $\sim(0.19:0.38:0.43)$.

⁵Another equivalent convention used in the literature is to report the dimensionless quantity $\mathcal{J} = J/\Delta\Omega R_0 \rho_0^2$ (Yüksel *et al.*, 2007).

⁶It is customary to specify $\rho_0 \equiv \rho_\chi(R_0)$ rather than ρ_s , as the former can be more directly measured. The two are related by inverting Eq. (5).

TABLE I. J factors for different experiments discussed in this review and their associated halo parameters. Given in units of $\text{GeV}^2 \text{cm}^{-5} \text{sr}$, the J factors are computed according to Eq. (2). We use these to find the expected neutrino flux as described in Eq. (1). Each row corresponds to a different experimental setup given its angular exposure. The first column names the experiment, the second column summarizes their angular acceptance, and the last three columns give the s -wave, p -wave, and d -wave J factors, respectively. Heart symbols indicate new results given in this review.

Experiment	Exposure	$J_s/10^{23}$	$J_p/10^{17}$	$J_d/10^{11}$
♥ All-sky	All-sky	2.3	2.2	3.6
♥ GRAND	Figure 24 of Alvarez-Muniz <i>et al.</i> (2018)	0.28	0.28	0.46
♥ ANITA	dec = $[1.5^\circ, 4^\circ]$	0.018	0.018	0.028
CTA (Queiroz, Yaguna, and Weniger, 2016)	Galactic Center (Queiroz, Yaguna, and Weniger, 2016)	0.074	0.12	0.16
♥ TAMBO	Figures 3 and 4 of Romero-Wolf <i>et al.</i> (2020)	0.0009
♥ Auger	Zenith = $[90^\circ, 95^\circ]$ Zenith = $[75^\circ, 90^\circ]$ Zenith = $[60^\circ, 75^\circ]$	0.10 0.28 0.27
♥ P-ONE	cos(zenith) = $[-1, -0.5]$ cos(zenith) = $[-0.5, 0.5]$ cos(zenith) = $[0.5, 1]$	0.87 1.2 0.13	0.85 1.2 0.12	1.4 2.0 0.18

B. Extragalactic contribution

In addition to DM annihilation in the MW, annihilation of extragalactic dark matter integrated over all redshifts should provide a diffuse isotropic neutrino signal (Beacom, Bell, and Mack, 2007). As in the search for extragalactic background light, there are two contributions to this isotropic flux: (1) a “background” flux from the diffuse (noncollapsed) distribution of DM whose rate grows with redshift as $\Omega_{\text{DM}}^2 \sim (1+z)^6$, and (2) a late-time contribution from the large overdensities in galactic halos.

In this case, the expected flux of neutrinos plus antineutrinos per flavor at Earth from DM annihilation is given by

$$\frac{d\Phi_{\nu+\bar{\nu}}}{dE_\nu} = \frac{1}{4\pi} \frac{\Omega_{\text{DM}}^2 \rho_c^2 \langle \sigma v \rangle}{\kappa m_\chi^2} \frac{1}{3} \times \int_0^{z_{\text{up}}} dz \frac{[1+G(z)](1+z)^3}{H(z)} \frac{dN_{\nu+\bar{\nu}}(E')}{dE'}, \quad (6)$$

where $H(z) = H_0[(1+z)^3 \Omega_m + (1+z)^4 \Omega_r + \Omega_\Lambda]^{1/2}$ is the time-dependent Hubble parameter, ρ_c is the critical density of the Universe, and Ω_m , Ω_r , and Ω_Λ are, respectively, the fractions of ρ_c made up of matter, radiation, and dark energy. While the upper limit on redshift z_{up} can in principle be as high as the neutrino decoupling time at $T \sim \text{MeV}$, neutrinos produced at that epoch are redshifted to the point of being invisible to existing detectors. $dN_\nu(E')/dE$ is the neutrino spectrum at the detector, where E' (E) is the energy at the source (detector). The spectrum is related to the source production spectrum via a Jacobian transformation to take cosmological redshift into account, namely,

$$\begin{aligned} \frac{dN_{\nu+\bar{\nu}}(E')}{dE'} &= 2 \frac{m_\chi}{E'^2} \delta\left(\frac{m_\chi}{E'} - 1\right) \\ &= \frac{2}{E} \delta\left[z - \left(\frac{m_\chi}{E} - 1\right)\right]. \end{aligned} \quad (7)$$

In Eq. (6), $\langle \sigma v \rangle$ is the thermally averaged cross section. The first part of the factor $1+G(z)$ in the integrand of Eq. (6) represents the isotropic background DM contribution, while $G(z)$ is the halo boost factor at redshift z . It accounts for the enhancement to the annihilation rate in DM clusters and their evolution with redshift and is given by

$$G(z) = \frac{1}{\Omega_{\text{DM},0}^2 \rho_c^2} \frac{1}{(1+z)^6} \times \int dM \frac{dn(M,z)}{dM} \int dr 4\pi r^2 \rho_\chi^2(r). \quad (8)$$

The first integral is over halo masses M , whose distribution is specified by the halo mass function (HMF) dn/dM , while the second integral is over the halo overdensities themselves. We model the latter as self-similar NFW profiles whose densities and radii are specified by a concentration parameter uniquely determined by their mass and redshift. The parametrization that we employ is based on fits to the MultiDark and BigBolshoi (Prada *et al.*, 2012) simulations and can be found in Appendix B of Lopez-Honorez *et al.* (2013).

Two uncertainties arise from the integral over M . The first is the choice of integration limits, specifically the lower limit M_{min} . This is because smaller halos are more concentrated and thus contribute more to the injected neutrino energy. This means that choosing arbitrarily low-minimum halo masses results in unrealistic limits. It is common in the literature to use $M_{\text{min}} = 10^{-6} M_\odot$ as a benchmark, although there is no data-driven motivation for this choice. M_{min} is not well constrained and will ultimately depend on model details (Cornell, Profumo, and Shepherd, 2013; Shoemaker, 2013). Therefore, in this review we pick $M_{\text{min}} = 10^{-3} M_\odot$ as a conservative limit choice. In Sec. IV.B, we show the effect of varying M_{min} down to $10^{-9} M_\odot$. The other uncertainty arises from the choice of HMF parametrization, dn/dM . We use the results of the N -body simulation by Watson *et al.* (2013), as parametrized

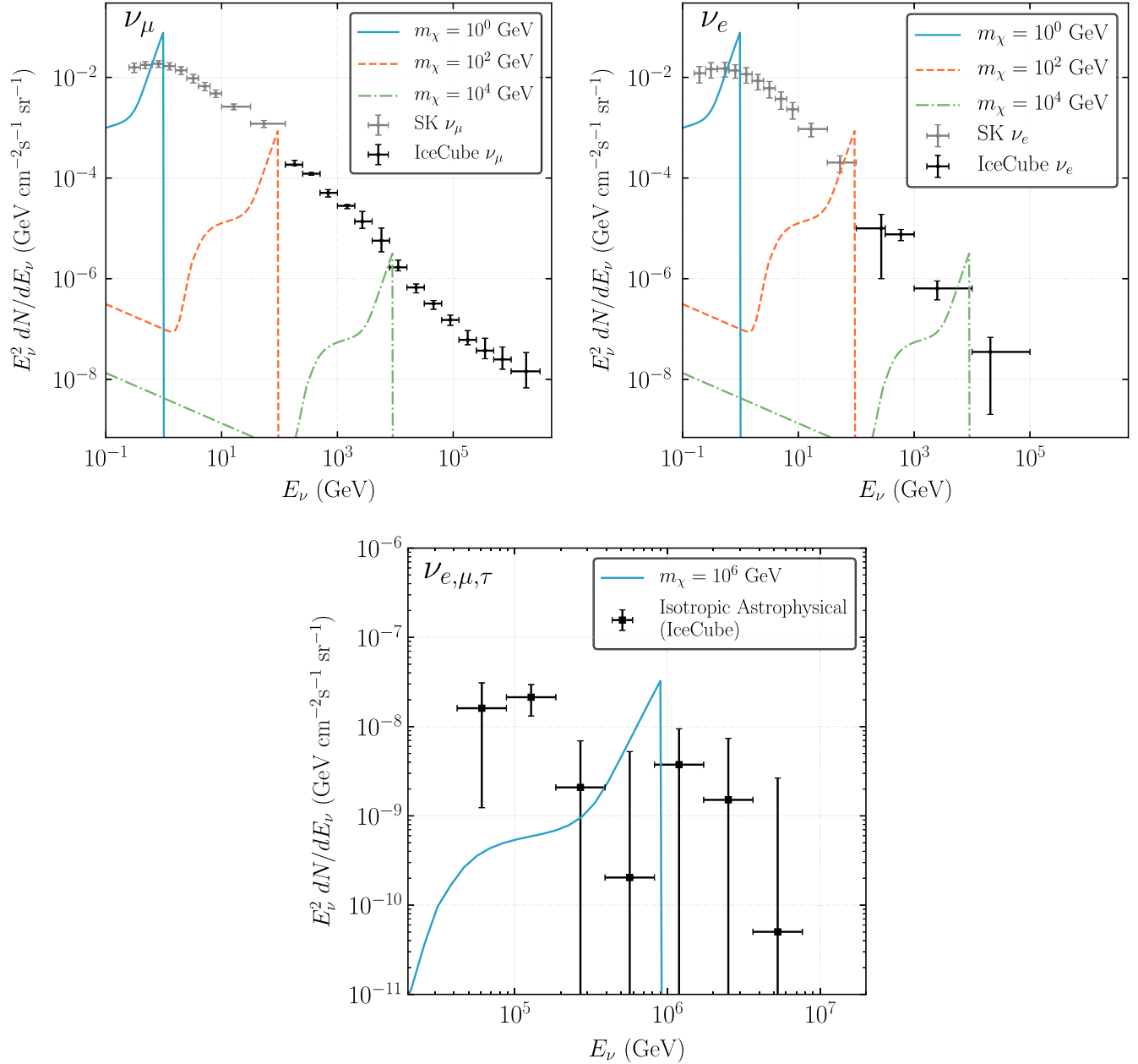


FIG. 1. Examples of neutrino fluxes produced by dark matter annihilation overlaid on the observed neutrino distributions. The expected flux of neutrinos from extragalactic dark matter annihilation as a function of energy is shown for several dark matter masses. Fluxes are computed using the value of the cross section corresponding to the 90% C.L. limit derived in this review. Here the extragalactic dark matter annihilation fluxes are compared to the unfolded atmospheric fluxes from both Super-Kamiokande (Richard *et al.*, 2016) and IceCube (Aartsen *et al.*, 2015b, 2016b). Top left panel: ν_μ channel. Top right panel: ν_e channel. Bottom panel: comparison to IceCube’s measured per-flavor isotropic astrophysical flux using 7.5 yr of starting events (Abbasi *et al.*, 2020).

by Lopez-Honorez *et al.* (2013) and Diamanti *et al.* (2014). Several other HMF parametrizations are tested, and the uncertainties due to the choice of HMF are quantified in Sec. IV.B.

The expected spectrum of DM annihilation to two neutrinos from cosmological sources is shown in Fig. 1 for different DM masses. These are overlaid on the Super-Kamiokande (SK) (Richard *et al.*, 2016) and IceCube (Aartsen *et al.*, 2015b; Aartsen *et al.*, 2016b) unfolded atmospheric ν_e and ν_μ fluxes as well as the isotropic astrophysical flux (Abbasi *et al.*, 2020).

C. Velocity-dependent annihilation

Certain matrix element vertex structures lead to a suppression of the constant (s -wave) part of the self-annihilation cross section. Expanded in powers of v/c , the dominant term may be p wave ($\propto v^2$) or d wave ($\propto v^4$) in the nonrelativistic limit. The DM velocity distribution depends on the kinematic details of the structure in which it is bound, as well as its distance from the center of that distribution. Assuming a normalized Maxwellian distribution $f(v, r)$ with dispersion $v_0(r)$, we find that the annihilation rate will be proportional to

$$\langle v^n \rangle = \int d^3v f(v, r) v^n. \quad (9)$$

For p and d waves, respectively, this yields

$$\langle v^2 \rangle = 3v_0^2(r), \quad (10)$$

$$\langle v^4 \rangle = 15v_0^4(r). \quad (11)$$

We obtain the dispersion velocity v_0 by solving the spherical Jeans equation while assuming isotropy. This is given by

$$\frac{d[\rho(r)v_0^2(r)]}{dr} = -\rho(r)\frac{d\phi(r)}{dr}, \quad (12)$$

where $\phi(r)$ is the total gravitational potential at radius r . For galactic constraints, we not only include the contribution of the DM halo to $\phi(r)$ but also follow [Boddy, Kumar, and Strigari \(2018\)](#) and include a parametrization of the MW bulge and disk potentials to account for their masses. These are given by

$$\phi(r)_{\text{bulge}} = -\frac{G_N M_b}{r + c_b}, \quad (13)$$

$$\phi(r)_{\text{disk}} = -\frac{G_N M_d}{r} (1 - e^{-r/c_d}), \quad (14)$$

where G_N is Newton's gravitational constant, $M_b = 1.5 \times 10^{10} M_\odot$ and $c_b = 0.6$ kpc are the bulge mass and scale radius, and $M_d = 7 \times 10^{10} M_\odot$ and $c_d = 4$ kpc are the disk mass and scale radius ([Boddy, Kumar, and Strigari, 2018](#)). Galactic J factors can then be reevaluated via

$$J_{v^n} = \int d\Omega \int_{\text{LOS}} \frac{\langle v^n(r) \rangle}{c^n} \rho_\chi^2(r) dx. \quad (15)$$

In the case of our extragalactic analysis, we only include the potential from the DM halos themselves. This is conservative in that the addition of the uncertain baryonic contributions would strengthen only our constraints. In a manner similar to the galactic case, Eqs. (6) and (9) must be modified to include the dependence on $\langle v^n \rangle(r)$. As long as the annihilation remains a two-to-two process [unlike the scenarios given by [Bell *et al.* \(2017\)](#)], Eq. (6) becomes

$$\frac{d\Phi_\nu}{dE_\nu} = \frac{c}{4\pi} \frac{\Omega_{\text{DM}}^2 \rho_c^2 \langle \sigma v \rangle}{2m_\chi^2} \int_0^{z_{\text{up}}} dz \frac{\{[(1+z)/(1+z_{\text{KD}})]^n + G_n(z)\}(1+z)^3}{H(z)} \frac{dN_\nu(E')}{dE}, \quad (16)$$

where the redshift z_{KD} is related to the temperature at kinetic decoupling T_{KD} and the temperature of the CMB today $T_{\text{CMB},0}$ via $1+z_{\text{KD}} = T_{\text{KD}}/T_{\text{CMB},0} \simeq 4.2 \times 10^9 (T_{\text{KD}}/\text{MeV})$ ([Diamanti *et al.*, 2014](#)). [Shoemaker \(2013\)](#) obtained the following temperature of kinetic decoupling:

$$T_{\text{KD}} \simeq 2.02 \text{ MeV} \left(\frac{m_\chi}{\text{GeV}} \right)^{3/4}. \quad (17)$$

In general, kinetic decoupling occurs later than chemical freeze-out and depends on the number of relativistic degrees of freedom $g_*(T_{\text{KD}})$. At redshifts where the annihilation products are still measurable by Earth-based detectors, the factor of $[(1+z)/(1+z_{\text{KD}})]^n$ still leads to a strong enough suppression that it will always be subdominant to the halo contribution proportional to $G_n(z)$. The exact value of T_{KD} in Eq. (17) is thus inconsequential. Equation (9) including velocity dependence is rewritten as follows:

$$G_n(z) = \frac{1}{\Omega_{\text{DM},0}^2 \rho_c^2} \frac{1}{(1+z)^6} \times \int dM \frac{dn(M, z)}{dM} \int dr 4\pi r^2 \frac{\langle v^n(r) \rangle}{c^n} \rho_\chi^2(r), \quad (18)$$

where we have used the same HMF as in the velocity-independent case, with the addition of the velocity dispersion $\langle v^n(r) \rangle$ in the rightmost integral. [Diamanti *et al.* \(2014\)](#) provided the detailed method of solving the Jeans equation to compute $\langle v^n(r) \rangle$ as a function of the DM halo

concentration. For convenience, we provide the following function for the p - and d -wave cases:

$$\ln(G_n) \simeq \sum_i c_i \alpha^i, \quad (19)$$

where c_i are the coefficients provided in Table II and $\alpha \equiv \ln(z)$. This parametrization is valid down to redshifts $\gtrsim 10^{-3}$.

III. EXPERIMENTAL METHODS

In this section we review the different methodologies and technologies used for neutrino detection relevant to the discussion of the experimental results discussed in this review. The results presented in Sec. IV rely on our understanding of the backgrounds in the region of interest. Depending on whether or not the background flux is known, upper limits can

TABLE II. Coefficients of the polynomial fit to velocity-dependent halo boost factors. The coefficients correspond to Eq. (19), which is a parametrization to the numerical solution of Eq. (21).

	p wave	d wave
c_0	-7.004	-19.88
c_1	-1.821	-2.493
c_2	-0.5793	-0.804
c_3	-0.095 59	-0.1636
c_4	-0.006 148	-0.021 01
c_5	0	-0.001 181

be either background agnostic or background informed. Moreover, the upper limits largely depend on the systematics that govern neutrino detection, for instance, the energy resolution and flavor identification capability. We first outline the statistical framework for limit setting before describing detector physics used over the energy ranges considered here, from a few MeV up to 10^{12} GeV and beyond.

A. Statistical methods

To contextualize the variety of experimental capabilities, we first outline the principal statistical treatments used to infer the properties of the flux of neutrinos from dark matter annihilation. We explain them in increasing order of complexity and strength.

1. Background-agnostic methods

In this method we use the observed data and the detector signal efficiency to constrain the flux of neutrinos from DM. This method can inform us of the maximum allowed flux, but, by construction, it cannot be used to claim the observation of dark matter. This technique is predicated on comparing the observed and expected number of events in a given bin by means of the following likelihood function:

$$\mathcal{L}(\mu) = \begin{cases} \mathcal{P}(d|\mu) & (d < \mu), \\ 1 & (d \geq \mu), \end{cases} \quad (20)$$

for which the likelihood is less than 1 only if the predicted number of events μ is larger than the recorded data d . The probability distribution \mathcal{P} could be a Poisson or Gaussian distribution depending on the sample size. Using this likelihood one can construct one-sided confidence upper limits on μ and, in turn, on the dark matter cross section given the J factor and detector acceptance. The strength of this method is determined by experiment exposure, signal efficiency, and the amplitude of unmodeled backgrounds; these determine the statistical uncertainty and the phase space over which the bins are defined. In the case of dark matter, one would ideally bin the events in energy, direction, and morphology; but often this is not done due to decreasing statistical power, insufficient Monte Carlo certainty, or increasing difficulty in modeling the systematic uncertainties.

In this review, we take advantage of this approach in a number of experimental settings. As examples, we compare the Super-Kamiokande unfolded neutrino energy distribution (Richard *et al.*, 2016) to the dark matter expectation using this technique and perform a similar comparison to the IceCube PeV astrophysical neutrino segmented fit. We also use this technique when experiments have not seen neutrino events and upper limits are reported, such as the Pierre Auger Observatory's limit on neutrino flux at very high energies.

2. Background-informed methods

A higher statistical power can be achieved by simultaneously modeling the signal (the event rate due to dark matter) and background (any other contribution to the observed rate). This requires signal and background efficiencies, as well as a

model for the background distribution over each observable. A prototypical likelihood function is

$$\mathcal{L}(\theta, \eta) = \mathcal{P}(d|\mu_s(\theta, \eta) + \mu_b(\eta))\Pi(\eta), \quad (21)$$

where $\mu_s(\theta, \eta)$ and $\mu_b(\eta)$ are the expected signal and background counts, respectively, d represents the observed counts, and θ and η are the dark matter parameters and nuisance parameters, respectively. The last parameters η incorporate the effect of the systematic uncertainties in the signal and background distributions and are often constrained by previous knowledge or *in situ* measurements represented in the function $\Pi(\eta)$. When the signal and background predictions are well defined, the probability function \mathcal{P} is taken to be a Poisson function in the small-count regime or a Gaussian function in the large-count regime.

If the signal or background predictions carry large uncertainties, which is often the case for rare backgrounds or signals that cover specific parts of phase space such as dark matter lines (Gainer *et al.*, 2014), stochastic likelihood models can be used (Argüelles, Schneider, and Yuan, 2019; Glüsenskamp, 2018, 2020). For other treatments proposed to tackle this problem see also Barlow and Beeston (1993), Chirkin (2013), and Bohm and Zech (2014).

In either case, the treatment of systematic uncertainties is often done by using the profile likelihood method, in which the likelihood function is maximized over the nuisance parameter at each physics parameter point (Heinrich and Lyons, 2007). Alternatively, in Bayesian treatments [see Trotta (2017)] or hybrid frequentist-Bayesian treatments (Cousins and Highland, 1992) the nuisance parameters are marginalized over by integrating the likelihood function. In a case in which the bin content is large, such that a Gaussian likelihood function is a good approximation, the expectations can be computed accurately. Often a multidimensional Gaussian is used where the covariance between bins incorporates both the systematic and statistical uncertainties. The latter approach does not require additional parameters to incorporate systematic uncertainties into the likelihood, making it computationally advantageous.

With this formalism, background-informed analyses have additional power relative to the background-agnostic scenario, provided that experiments are capable of constraining the background size and separating it from signal. The ability to constrain the background is encapsulated in systematic uncertainties, whereas the separation of background from signal depends on the features of both. The features in the case of neutrinos from dark matter are a democratic flavor composition, spatial clustering predominantly around the Galactic Center, and an energy distribution that is maximal close to the dark matter mass. Separating dark matter from background using these three features then depends on the experimental direction and energy resolutions, as well as its flavor identification capabilities dictated by the event morphological classification. The last feature is important since natural and anthropogenic sources often have a nondemocratic flavor composition. This is a characteristic of the stronger constraints. For example, we use the fact that for MeV dark matter one of the main backgrounds consists of solar

neutrinos, which can be efficiently removed by selecting only for antineutrinos in Super-Kamiokande or Jiangmen Underground Neutrino Observatory (JUNO); we also rely on this in our predictions of the sensitivities for DUNE and Hyper-Kamiokande in the 100 MeV to 30 GeV energy range, where we use the fact that one can perform morphological event analysis to remove muon neutrinos, which are the dominant component of the atmospheric flux.

B. Neutrino detection methods

Because neutrinos interact only via the weak nuclear force, neutrino detection must proceed in at least two steps: first, interaction between a neutrino and a detector electron or nucleus and, second, the detection of the resulting electromagnetic signal. Typically, energy from a gamma ray or electron cascades down via scintillation, additional ionization, or Cherenkov radiation and is subsequently measured by optical sensors or charge readout.

The small neutrino detection cross section poses a significant challenge in the search for the expected fluxes from dark matter annihilation to neutrinos. As the dark matter mass increases, larger detectors are necessary to compensate for the smaller flux, which scales as m_χ^{-2} . Such a scaling can come at the cost of energy and angular resolution as well as flavor identification, all of which allow differentiation between the dark-matter-induced neutrinos from other natural or anthropogenic neutrino sources, as discussed in Sec. III.A. In this section, we review the techniques used to detect neutrinos in different energy ranges; see also Katori and Martini (2018) and Diaz *et al.* (2019) for a discussion in the context of neutrino oscillation experiments. Note that the energy ranges detailed here are approximate, and there is some overlap between the techniques and physics discussed in each respective section.

1. Neutrino energies below 10 MeV

Coherent elastic neutrino-nucleus scattering, namely, $\nu A_N^Z \rightarrow \nu A_N^{*Z}$, dominates the cross section at the lowest energies (Freedman, 1974). This process, sometimes abbreviated as CE ν NS, has no kinematic threshold and scales quadratically with the atomic number. However, the maximum recoil energies are small, making its detection difficult; in fact it has only recently been observed using anthropogenic neutrinos in detectors of $\mathcal{O}(10)$ kg of mass (Akimov *et al.*, 2017). Future ton-scale dark matter direct detection experiments such as DARWIN (Aalbers *et al.*, 2016) expect to see solar and atmospheric neutrinos via CE ν NS. Because of the trade-off between detector size and nuclear recoil threshold, they would be sensitive to DM only above $m_\chi \sim 10$ MeV and provide only a marginal improvement over existing dedicated neutrino experiments that use different detection channels.

Neutrino-electron scattering also has no kinematic threshold at detectable energies, and the cross section is predicted without ambiguities that arise from form factors in hadron-neutrino interactions. This interaction's well-understood kinematics, together with the fact that a single outgoing charged particle is produced, makes it a good channel to use for DM annihilation searches. This is because precise energy and

directional information can be inferred. The angle between the neutrino and the electron is tightly constrained by the kinematics ($E_e \theta_e < 2m_e$), allowing for an accurate reconstruction of the neutrino direction. [It was through this process that in 1998 the Super-Kamiokande experiment made the first image of the Sun in neutrinos (Fukuda *et al.*, 1998); see also Ahmad *et al.* (2001), Alimonti *et al.* (2002), and Arpesella *et al.* (2008) for subsequent measurements by SNO and Borexino.] Angular information is used to mitigate the ~ 1 –10 MeV solar neutrino backgrounds and to search for correlations with the expected angular distribution of DM via $J(\Omega)$. The neutrino-electron cross section is approximately 10^{-43} cm² at 5 MeV, which is about a factor of 10 smaller than the dominant neutrino-nucleon process.

The other commonly used technique to detect sub-10 MeV neutrinos is inverse beta decay (IBD): $\bar{\nu}_e p \rightarrow n e^+$. This is due to three reasons: first, the large and well-measured IBD cross section, approximately 10^{-42} cm at 5 MeV (Vogel and Beacom, 1999; Ankowski, 2016), with an uncertainty of $\sim 0.2\%$ (Vogel and Beacom, 1999; Kurylov, Ramsey-Musolf, and Vogel, 2003); second, the low threshold: $E_\nu > 1.806$ MeV; and, finally, the ability to reduce background by searching for the prompt positron signature followed by the neutron capture. This detection method is often used with hydrocarbon-based scintillator since it contains a large number of free protons and emits a large number of photons, typically 10^4 per MeV of deposited energy (Leo, 1994). The energy deposited by the prompt signal is the kinetic energy of the positron plus two 511 keV gamma rays from electron-positron annihilation, and a 2.2 MeV gamma ray from the delayed capture of the neutron on free protons. In hydrogen-based detectors the neutron capture time is typically 300 μ s. If the detector is doped with 1% gadolinium, this time is reduced to about 20 μ s and the prompt gamma-ray energy is 8 MeV, allowing for an improved background suppression (Beacom and Vagins, 2004); e.g., in the case of Super-Kamiokande a hundredfold background suppression efficiency can be achieved (Watanabe *et al.*, 2009). In the search for dark matter this process has the advantage that it is triggered only by $\bar{\nu}_e$, allowing for efficient suppression of the solar neutrino flux that dominates the natural backgrounds at sub-10 MeV energies. In fact, our strongest limit across all dark matter masses comes from an IBD search by Super-Kamiokande; see Fig. 2.

2. Neutrino energies between 10 MeV and 1 GeV

Between ~ 10 MeV and ~ 1 GeV, in Cherenkov detectors the proton is invisible since it is Cherenkov threshold: approximately 1.3 GeV in mineral oil, 1.4 GeV in water, and as low as 1.2 GeV in the Antarctic ice (Besson *et al.*, 2012). This has advantages and disadvantages relative to scintillator detectors. On the one hand, it simplifies identification and classification of events since the observed Cherenkov light must be associated with the outgoing charged lepton. On the other hand, the lack of proton kinematics means that the energy and angular resolution can be significantly degraded. The dominant neutrino-nucleon process in this energy range is that of charged-current quasielastic (CCQE) scattering, namely, $\nu_\alpha N \rightarrow \alpha \tilde{N}$, where α is a charged lepton

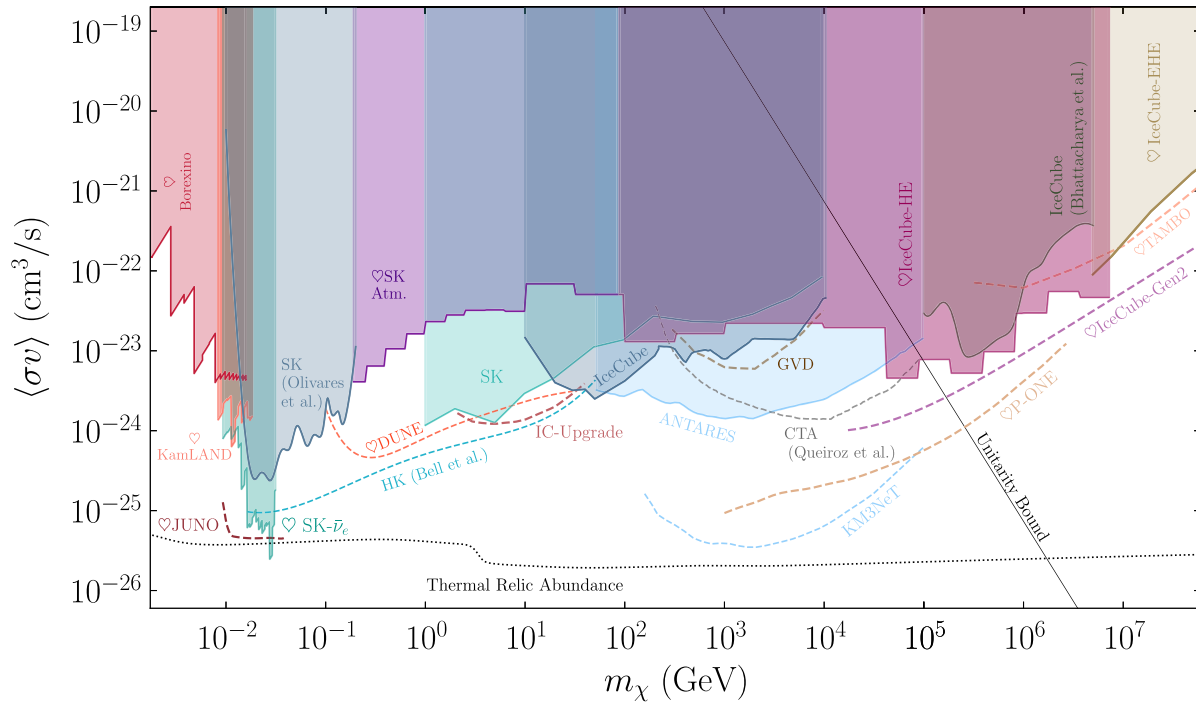


FIG. 2. Landscape of dark matter annihilation into neutrinos up to 10^8 GeV. We show results from this review, as well as previously published limits. Data and corresponding references are detailed in Sec. IV. Solid and dashed lines represent 90% C.L. limits and sensitivities, respectively. Projected sensitivities assume 5 yr of data taking for neutrino experiments and 100 h of observation for CTA. The dotted line corresponds to the value required to explain the observed abundance via thermal freeze-out. The straight diagonal line, labeled “unitarity bound,” gives the maximum allowed cross section for a noncomposite DM particle. These results assume that 100% of the dark matter is composed of a given Majorana particle. If instead only a fraction f is considered, these results should be multiplied by $1/f^2$. In the case of Dirac DM, limits would be scaled up by a factor of 2. The heart symbols indicate new results obtained in this review. See Fig. 4 for constraints and projections up to 10^{11} GeV.

and N (\tilde{N}) is a proton or neutron. At high enough energies, muon neutrinos can have CCQE interactions, producing muons that can be identified by the morphology of the Cherenkov ring. Because of the larger mass, muons tend to preserve their direction as they travel through the detector, producing sharper rings than electrons. Cherenkov detectors can be constructed out of mineral oil, water, or ice. Although oil-based detectors boast a larger Cherenkov angle and the ability to run without a purification system, they are utilized only in smaller detectors (Diaz *et al.*, 2019) due to the higher filling cost. For this reason, multikiloton detectors available as of 2020 are all water or ice based. As early as 2022, JUNO will become the first multikiloton liquid scintillator detector. Since the DM-induced flux is expected to be small, the larger water or ice Cherenkov detectors currently dominate the constraints over oil-Cherenkov detectors, and we do not discuss them further here.

3. Neutrino energies from 1 to 10^7 GeV

Resonant light-meson production is important between approximately 1 and 10 GeV. Because of the difficulty in cross-section modeling, neutrino detection in this range is subject to large uncertainties. Above 10 GeV the contribution of deep inelastic scattering (DIS), where the neutrino exchanges a W or Z boson with one of the partons inside, the nucleon becomes the dominant process. The production of

taus in tau-neutrino charged-current interactions becomes possible above the threshold $m_\tau = 1.777$ GeV, although the cross section is only around 15% of the charged-current muon-neutrino cross section at 10 GeV, rising to 75% at 100 GeV (Conrad *et al.*, 2010).

Although unsegmented Cherenkov detectors are still used in this energy range, the use of tracking calorimeters, often constructed as segmented scintillators, are popular, as they allow for improved reconstruction of outgoing muon tracks, as well as electromagnetic and hadronic showers produced in the interaction vertex. Notable examples of these types of detectors in contemporary neutrino physics are the NO ν A experiment and the T2K near detector. Sampling calorimeters have also been used to increase the target density, although this comes at the expense of a degraded energy resolution. In this case a dense material like iron is interleaved with scintillator panels. This design was used by the MINER ν A experiment (Aliaga *et al.*, 2014) to perform precision measurements of the neutrino cross section and was used in the past to measure neutrino oscillations by MINOS (Sousa, 2015). In these detectors the morphological features observed in the trackers have been used to identify the different neutrino interaction processes by comparing them to generated event libraries (Sousa, 2007; Backhouse and Patterson, 2015) or convolutional neural networks (Aurisano *et al.*, 2016; Psihas *et al.*, 2019). Given the size of these detectors they are not expected to play a role

in the detection of dark matter and are not included in this review.

The newest neutrino detectors in this energy range are the so-called liquid argon time projection chambers (LARTPCs) (Cavanna, Ereditato, and Fleming, 2018). These detectors consist of an electric field cage filled with liquid argon. When a charged particle is produced in the argon, it travels through the medium and ionizes the argon atoms, thereby liberating the electrons. An electric field then drifts the electrons to wire planes on one side of the detector, recording a projected footprint of the interaction. Three-dimensional reconstruction is also possible by using the timing of the charge deposition on the wires. To localize the event in the third dimension, the drift time of electrons in argon and the initial interaction time need to be known. The initial interaction time can be known in the case of generic neutrino interactions via the scintillation light produced by the charged particles in argon or, in the case of neutrinos produced in bunches in a beam, by the beam timing. In the case of dark matter searches, relevant for this review, only the former technique is relevant. Even though the neutrino-argon cross section is currently poorly understood compared to other materials conventionally used in neutrino physics, these detectors have the potential for unprecedented particle identification; see Acciarri *et al.* (2018), MicroBooNE Collaboration (2018), and Adams *et al.* (2019)). Examples of currently operating LARTPC neutrino detectors are MicroBooNE (Acciarri *et al.*, 2017) and ICARUS (Ali-Mohammadzadeh *et al.*, 2020) at Fermilab. The next-generation experiment in this category is DUNE (Abi *et al.*, 2020b).

At the higher end of this energy range, neutrino telescopes such as ANTARES and IceCube have the largest neutrino collection volumes. These detectors operate at energies above 10 GeV where DIS is the dominant cross-section process (Gandhi *et al.*, 1996). These detectors use natural media, such as the Mediterranean water or the Antarctic ice, as targets for the neutrino interaction. Cherenkov light produced by charged particles by products of these interactions are then observed by photomultiplier tubes arranged on sparse arrays. In these detectors the different neutrino interactions map onto different morphologies of the time and spatial distribution of charge in the array. Neutral-current interactions, charged-current electron-neutrino interactions, and most of the charged-current tau-neutrino interactions produce a morphology known as a cascade. Because cascades can be contained in the detector, this morphology has the best energy resolution. Charged-current muon-neutrino interactions produce a morphology known as tracks due to the long travel time of the muon. This morphology provides the best directional information. In water, photons tend to scatter less than in ice, providing more direct light. This means that the muon angular resolution in water-based detectors is better than those in ice. On the other hand, given the longer absorption length of photons in ice than in water, the effective detector volume is larger for detectors deployed deep in the ice. Finally, charged-current tau-neutrino interactions can produce a variety of morphologies depending on the boost factor of the tau and its decay channel. For example, at around 1 PeV a tau can travel on average 50 m before decaying and producing separated energy depositions known as double bangs (Learned and Pakvasa, 1995; Cowen,

2007); in 2018 IceCube announced the first candidate astrophysical tau events (Stachurska, 2018, 2020). Finally, in these detectors one can also observe the electron-neutrino scattering since, at approximately 6.3 PeV, an electron antineutrino can resonantly scatter, with an atomic electron producing a W on shell (Glashow, 1960; Loewy, Nussinov, and Glashow, 2014). W production of coherent photon scattering can also be important at these energies; see Seckel (1998), Alikhanov (2016), Garcia *et al.* (2020), and Zhou and Beacom (2020a, 2020b). The observation of this process provides a unique handle on the ratio of neutrinos to antineutrinos and also provides exquisite energy resolution; in fact, a candidate event has recently been detected (Lu, 2019).

4. Neutrino energies above 10^7 GeV

At extremely high energies, the neutrino flux expected from dark matter and other astrophysical sources such as cosmogenic neutrinos is small, necessitating the construction of detectors with effective volumes much larger than a cubic kilometer. Neutrino interactions in this energy range occur overwhelmingly via deep inelastic scattering (Gandhi *et al.*, 1996). Two main techniques are used to search for neutrinos in this energy range, both of which rely on identifying horizontal or upgoing particles to mitigate the larger cosmic-ray backgrounds. The first method involves looking for air showers induced by neutrino-nucleus interactions in the atmosphere or just below the surface of Earth, while the second uses the radio signature produced in very-high-energy neutrino interaction (Gusev and Zheleznykh, 1984; Markov and Zheleznykh, 1986), known as Askaryan radiation (Askaryan, 1962; Zas, Halzen, and Stanev, 1992).

The former technique can be detected in a number of ways: sparse surface arrays of water-Cherenkov tanks are used to identify charged particles from showers as they develop over an area that may span many square kilometers. Air fluorescence telescopes and optical air Cherenkov telescopes can also be used alone or in combination with water tanks [as is the case for the Pierre Auger Observatory (Aab *et al.*, 2015b)]. The timing, morphology, and amount of light deposition is used to infer the energy of the incoming particle, its direction, and its nature. In particular, a neutrino will typically travel much deeper into the atmosphere than a cosmic ray or gamma ray before interacting. Tau neutrinos are particularly promising, as τ leptons can be produced in a nearby mountain or below the horizon (Jeong *et al.*, 2017). If the tau survives the journey out of the mountain, its decay yields an upgoing air shower (Reno, Krizmanic, and Venters, 2019; Reno *et al.*, 2020); an EeV τ typical interaction length is a few kilometers in rock and is shorter than its decay length. The expected event rate for such processes at cosmic-ray observatories like Auger turns out to be higher than from neutrino-induced atmospheric showers, thanks to the high density of rock. Radio arrays such as GRAND (Alvarez-Muniz *et al.*, 2018) have been proposed to cover as large an effective area as possible (up to 200 000 km²) to search for such a signal.

The second method, Askaryan radiation detection, aims to observe neutrinos via the radio emission generated by charge displacement caused by the developing electromagnetic or hadronic shower after DIS scattering. This emission is distinct

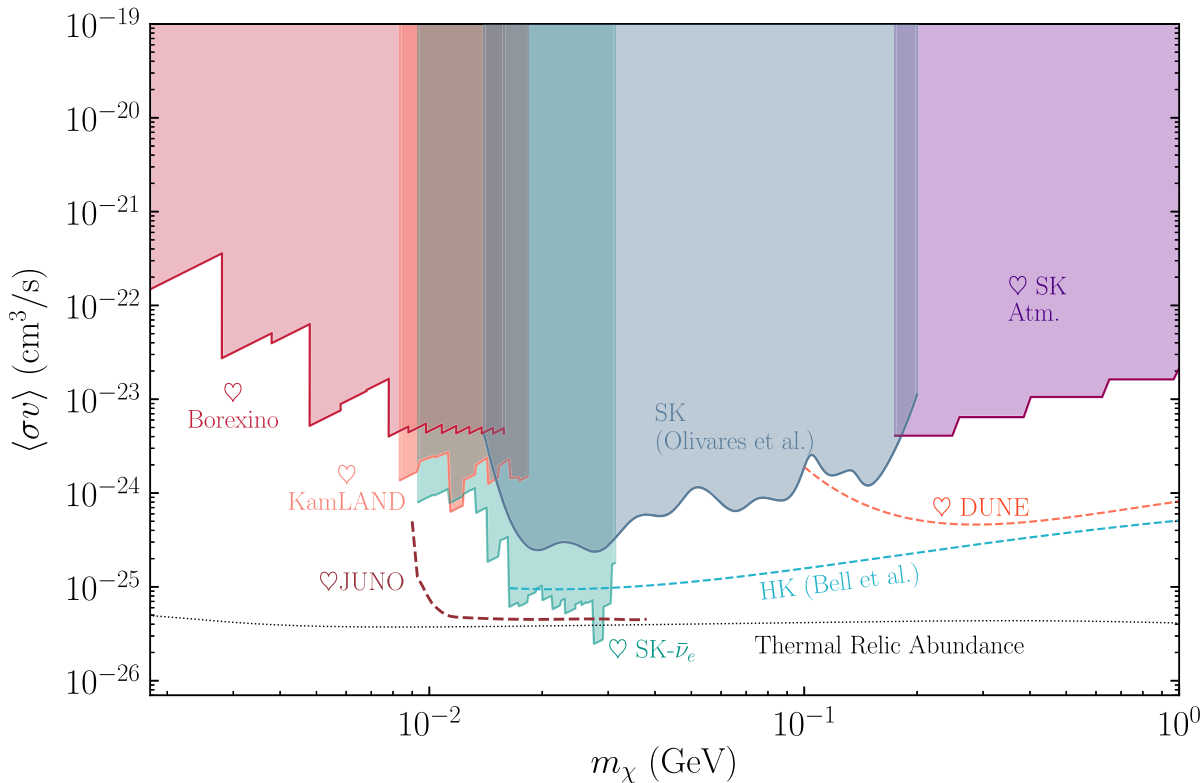


FIG. 3. Landscape of sub-GeV dark matter annihilation into neutrinos. The same as Fig. 2, but restricted to dark matter masses below 1 GeV.

from down-going cosmic-ray showers in that the polarization of the radio signal is expected to be different. This technique has been implemented by using radio antennas that are either suspended from balloons (Gorham *et al.*, 2010) or buried in the ice (Allison *et al.*, 2019; Anker *et al.*, 2020) on the Antarctic continent. The ability to cover a large area with a single antenna cluster makes this a scalable and relatively low-cost technique.

IV. RESULTS

Our main results are shown in Figs. 2–6. Figure 2 shows the results derived according to the procedures described in Secs. II.A and II.B, in addition to previous results available in the literature. Figure 3 shows a more detailed view of the low-mass (sub-GeV) range; Fig. 4 shows results for the high-mass (10^3 – 10^{11} GeV) region. Finally, Figs. 5 and 6 provide the constraints and projections in the case of velocity-dependent p -wave and d -wave annihilation, respectively. We label the results derived specifically for this review with a heart symbol.

In the rest of this section, we describe the data that we used to produce or recast limits on DM annihilation into neutrinos according to the procedures outlined in Sec. II. We split the data into three lists: (1) data used to construct constraints in Fig. 2, (2) previous limits that we have recast, and (3) data used to place limits in the high-mass ($m_\chi > 10^3$ GeV) region.

When reporting literature results, where possible we have rescaled them to use the same halo parameters, i.e., consistent J factors, as computed in Sec. II.A. In this way, we ensure that

the constraints we present can be properly compared with one another. The rescaling could not be done in the case of ANTARES (Adrian-Martinez *et al.*, 2015), SK (Frankiewicz, 2017), or IceCube (Aartsen *et al.*, 2016a), since these were event-by-event analyses for which data are not publicly available. This is unfortunate since the halo parameters used in these studies are no longer preferred; see the discussion in Sec. IV.B. Shaded regions correspond to experimental limits, whereas dashed lines are projections based on future experimental sensitivity. Finally, we include two lines for reference. First, the dotted black line in Fig. 2 corresponds to the cross section required to produce the observed relic abundance from thermal freeze-out computed as in Steigman, Dasgupta, and Beacom (2012) and, second, the solid black line labeled “unitarity bound” corresponds to the perturbative unitarity limit on noncomposite WIMP dark matter (Griest and Kamionkowski, 1990); see Smirnov and Beacom (2019) for a recent discussion.

The limits shown in Fig. 2, employing the approach of Secs. II.A and II.B, use the following data, which we also summarize in Table III.

- (1) *Borexino*.—Borexino is a large-volume unsegmented liquid scintillator detector located underground at the Laboratori Nazionali del Gran Sasso in Italy (Alimonti *et al.*, 2009). The Borexino Collaboration has released two event selections: one that has a lifetime of 736 days selecting electron-antineutrino candidate events over the entire fiducial volume and another one with 482 days of lifetime designed to search for geoneutrinos (Bellini *et al.*, 2010). These event selections are

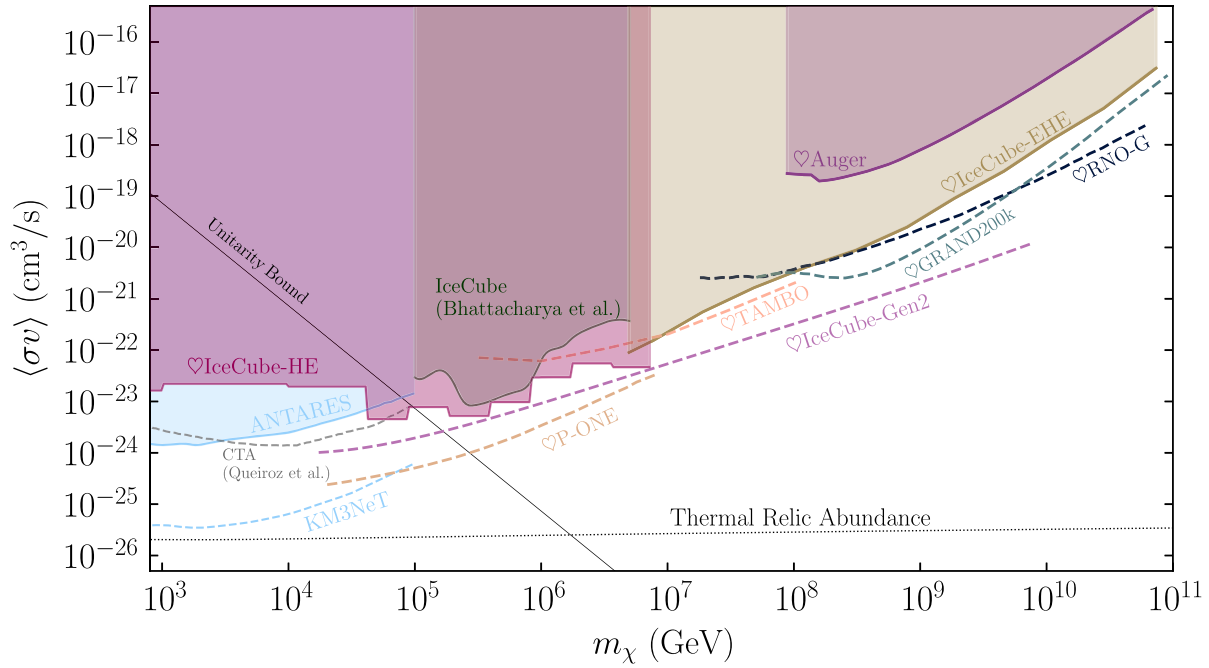


FIG. 4. Landscape of supra-TeV dark matter annihilation into neutrinos. The same as Fig. 2, but for the high-mass region. All the experimental constraints are calculated by converting either the detected flux or the reported upper limit into a conservative upper bound on the DM annihilation cross section.

combined into a single set designed to obtain a pure sample of electron antineutrinos by means of searching for signatures of inverse beta decay. Using this selection, they derive upper limits on the all-sky

monochromatic electron-antineutrino flux ranging from $\sim 10^5$ to $\sim 10^2 \bar{\nu}_e \text{ cm}^{-2} \text{ s}^{-1}$ for energies ranging from ~ 2 to 17 MeV, respectively. We use the flux upper limits produced by Bellini *et al.* (2011) and

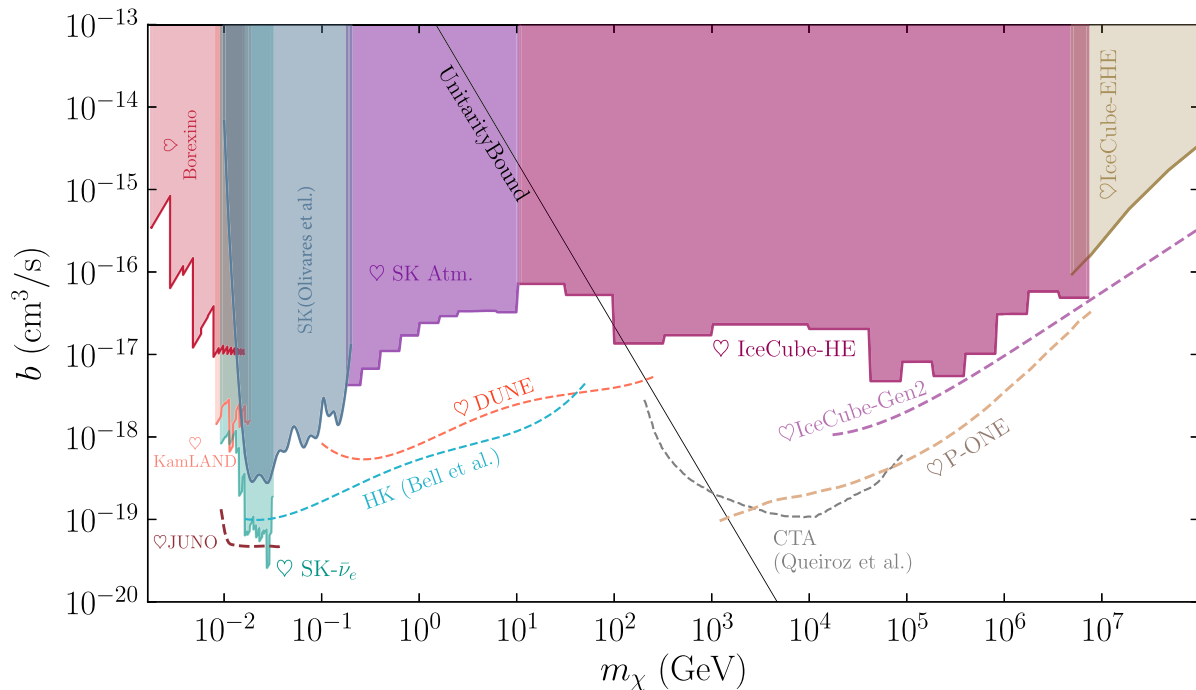
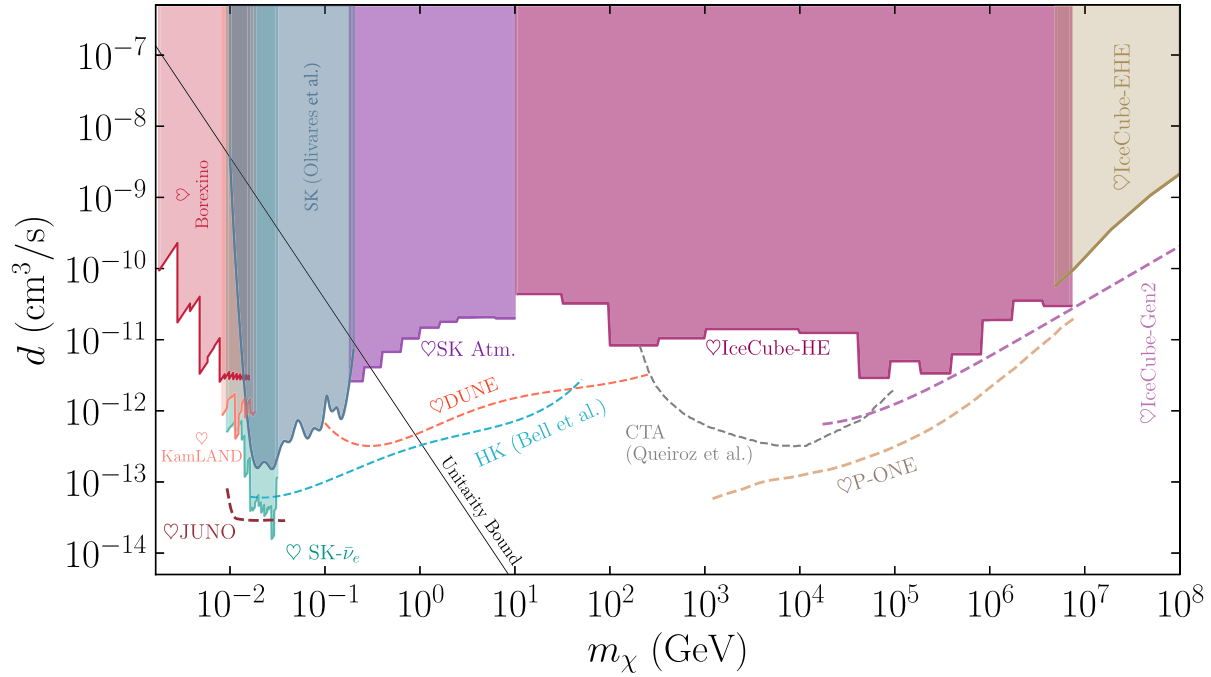


FIG. 5. Limits on p wave $\langle\sigma v\rangle = b(v/c)^2$, velocity-dependent annihilation cross section of dark matter to two neutrinos. The cross section needed to explain the observed abundance for thermal DM is $\langle\sigma v_r\rangle = 6 \times 10^{-26} \text{ cm}^3/\text{s}$.


 FIG. 6. Limits on the annihilation of neutrinos to dark matter through a d -wave process $\langle\sigma v\rangle = d(v/c)^4$.

recently updated by [Agostini *et al.* \(2019\)](#) and compare it to one-sixth of the all-flavor expected flux from dark matter to set our constraints.

- (2) SNO+ (*not shown*).—SNO+, located at the SNOLAB underground facility in Sudbury, Ontario, Canada, consists of a 12 m diameter acrylic vessel that will ultimately be filled with 780 tonnes of liquid scintillator and 800 kg of ^{130}Te , with the goal of searching for neutrinoless double-beta decay ([Andringa *et al.*, 2016](#)). Recent measurements in the water phase of SNO+ searching for invisible proton decay channels

have been performed ([Anderson *et al.*, 2019](#)). The event selection of this analysis looks for an atomic deexcitation into two gammas prompted by proton decay for a period of 114.7 days. For energies below ~ 6 MeV the observed rate is well described by internal backgrounds produced by ^{214}Bi and ^{208}Ti decay chains; at higher energies they are dominated by electron antineutrinos from nearby nuclear reactors interacting with atomic electrons. Neutrinos produced by dark matter can induce a similar signal when they have neutral-current interactions with the

TABLE III. Summary of current and future experiments discussed in this review for different energy ranges. Also indicated is whether the experimental analysis used directional information and which neutrino flavors it relied on. IC, IceCube.

Energy range	Experimental analysis	Directionality	Detected flavor
2.5–15 MeV	Borexino (Bellini <i>et al.</i>, 2011)	✗	$\bar{\nu}_e$ (IBD)
8.3–18.3 MeV	KamLAND (Gando <i>et al.</i>, 2012)	✓	$\bar{\nu}_e$ (IBD)
10–40 MeV	JUNO (An <i>et al.</i>, 2016)	✓	$\bar{\nu}_e$ (IBD)
15– 10^3 MeV	SK (Olivares-Del Campo <i>et al.</i>, 2018) DARWIN (McKeen and Raj, 2018)	✗	$\bar{\nu}_e$ (IBD) All flavors (coherent)
0.1–30 GeV	DUNE (Abi <i>et al.</i>, 2020b) HK (Olivares-Del Campo, Palomares-Ruiz, and Pascoli, 2018)	✗	$\nu_e, \bar{\nu}_e, \nu_\tau, \bar{\nu}_\tau$ (CC)
1– 10^4 GeV	SK (Frankiewicz, 2015; Abe <i>et al.</i>, 2020)	✓	All flavors
20– 10^4 GeV	IceCube (Aartsen <i>et al.</i>, 2016a)	✓	All flavors
50– 10^5 GeV	ANTARES (Adrian-Martinez <i>et al.</i>, 2015)	✓	$\nu_\mu, \bar{\nu}_\mu$ (CC)
0.2–100 TeV	CTA (Queiroz, Yaguna, and Weniger, 2016)	✓	All flavors (bremsstrahlung)
10– 10^4 GeV	IC Upgrade (Baur, 2019)	✓	All flavors
> 10 PeV	IC Gen2 (Aartsen <i>et al.</i>, 2014b)	✓	All flavors
10– 10^4 TeV	KM3Net (Adrian-Martinez <i>et al.</i>, 2016)	✓	All flavors
1–100 PeV	TAMBO (Wissel <i>et al.</i>, 2019)	✓	$\nu_\tau, \bar{\nu}_\tau$ (CC)
> 100 PeV	GRAND (Alvarez-Muniz <i>et al.</i>, 2018)	✓	$\nu_\tau, \bar{\nu}_\tau$ (CC)

medium. We computed the distribution of electron recoils in neutrino-electron charged-current interactions (Berestetskii, Pitaevskii, and Lifshitz, 1974; Formaggio and Zeller, 2012) and compared the expected rate to the observed sample rate given by Anderson *et al.* (2019). The resulting limits from 5 to 30 MeV, assuming 100% electron detection efficiency, lie above $\langle\sigma v\rangle \gtrsim 10^{-20} \text{ cm}^3 \text{ s}^{-1}$. We do not include this line in our figures, as the inclusion of realistic efficiencies, which are not publicly available, will push these limits up. Depending on the tellurium-loading schedule, an extended scintillator-only run could substantially improve these limits.

- (3) *KamLAND*.—KamLAND is an unsegmented liquid scintillator detector located in the Kamioka observatory near Toyama, Japan. The approximately 1 kt of mineral oil fiducial volume is contained in a 13 m balloon. Beyond its well-known work on reactor neutrinos, KamLAND has measured the ^8B solar spectrum (S. Abe *et al.*, 2011), searched for geoneutrinos (Gando *et al.*, 2013), and placed limits on the flux of extraterrestrial neutrinos above ~ 8.3 MeV (Gando *et al.*, 2012) which constrains the supernovae relic neutrino flux. In the last work, an upper limit on the extraterrestrial flux of $\bar{\nu}_e$ is derived, which is at the $\mathcal{O}(10)\bar{\nu}_e \text{ cm}^{-2} \text{ s}^{-1} \text{ MeV}^{-1}$ level and is given from 8.3 to 18.3 MeV. Using this result, we derive a constraint on the dark matter annihilation into neutrinos, shown in salmon in Fig. 2. Note that in Gando *et al.* (2012) the KamLAND Collaboration derived a similar constraint, but with outdated J factors; their result and ours are comparable. These are the leading constraints in the ~ 10 MeV mass range, but we expect that they will be improved by the next-generation liquid scintillator detector in China, JUNO (An *et al.*, 2016).
- (4) *Super-Kamiokande*.—SK is a 50 kt ultrapure water-Cherenkov detector located in Kamioka, Japan (Fukuda *et al.*, 2003). SK can use the morphology of the Cherenkov ring produced by charged particles to perform particle identification and energy measurement and obtain directional information of the events. The unfolded electron- and muon-neutrino fluxes in the sub-GeV to several TeV energy range was published by SK (Richard *et al.*, 2016). This unfolding uses data from the four stages, SK-I, SK-II, SK-III, and SK-IV, resulting in a total lifetime of 4799 days for the fully contained and partially contained event selection and 5103 for the upward-going muon sample. The unfolded fluxes are expected to be dominated by the atmospheric neutrino flux; in fact they are in agreement with model predictions such as the Honda-Kajita-Kasahara-Midorikawa model (Honda *et al.*, 2007) within systematic uncertainties. The dominant source of uncertainties on the unfolded fluxes is the neutrino interaction cross section, which introduces an uncertainty of approximately 20% in the unfolded flux. In the case of electron neutrinos, the second largest uncertainty is due to the small statistics at high energies, which can be up to 10% in the highest energy

bins. For all flavors, all other sources of uncertainty are less than 5% across all energy bins. We compare the unfolded flux to the expected flux from dark matter to produce limits on galactic and extragalactic dark matter annihilation. These results are shown in purple in Figs. 2, 5, and 8, and labeled with a heart symbol plus “SK-Atm.” To obtain these limits we used the background-agnostic approach described in Sec. III.A, and a binned truncated Gaussian likelihood in energy with 2 degrees of freedom. This result is complementary with SK galactic dark matter annihilation analysis (Frankiewicz, 2017, 2018; Abe *et al.*, 2020), shown in teal in Fig. 2 and simply labeled “SK.” As expected, our limits using the background-agnostic method are weaker than ones produced by the collaboration, but our analysis extends to lower energy and covers the energy range from 0.1 to 100 GeV in dark matter mass. Additionally, we perform an analysis using 2853 days of low-energy data from SK-I, SK-II, and SK-III, as well as 2778 days of data from SK phase IV, which led to an upper limit on the relic supernova electron-antineutrino ($\bar{\nu}_e$) flux (Linyan, 2018) labeled with a heart symbol plus “SK- $\bar{\nu}_e$.” The resulting limits on $\langle\sigma v\rangle$ turn out to be the strongest over the entire mass range that we consider, flirting with the relic abundance line for masses between 27 and 30 MeV.

- (5) *IceCube*.—The IceCube Neutrino Observatory is a gigaton ice Cherenkov neutrino detector located at the geographic South Pole (Aartsen *et al.*, 2017c). IceCube has measured the atmospheric neutrino spectrum in the 100 GeV to 100 TeV energy range. By separating the events into their observed morphologies (“cascades” and “tracks”), the collaboration recently published the unfolded electron- and muon-neutrino flux in this energy range (Aartsen *et al.*, 2015b, 2016b). At energies greater than 60 TeV, using events whose interaction vertex starts in the inner part of the detector (Aartsen *et al.*, 2013; Schneider, 2019) they also reported the result of a piecewise power-law fit to the astrophysical neutrino component using more than 6 yr of data (Aartsen *et al.*, 2017a). We use these to produce background-agnostic limits on the velocity-averaged dark matter annihilation cross section by comparing the produced neutrino flux to the reported unfolding or spectral fits. The obtained limits are shown for dark matter masses from 200 GeV to 10 PeV, labeled with a heart symbol plus “IceCube-EHE” and colored in dark magenta. Limits use the same likelihood construction as in the case of the previously described SK limits. Note that the muon-neutrino atmospheric unfolding reported by IceCube uses northern tracks, which are in the wrong hemisphere for the Galactic Center. Therefore, for that sample we constrain extragalactic emission only. Dedicated neutrino-line searches have not been yet performed by the IceCube Collaboration, although sensitivities were estimated by El Aisati *et al.* (2017, 2018) to be stronger than current IceCube constraints in that region. We describe the region labeled “IceCube-EHE” as part of the description of the high-mass region.

Additionally, we use the following previously published limits on dark matter annihilation obtained by constraining the galactic flux, rescaled to account for the galactic halo parameters used here unless indicated otherwise.

- (1) *Super-Kamiokande diffuse supernovae flux search.*—The gray region in Fig. 2 labeled “SK (Olivares *et al.*)” is an independent analysis of SK all-sky low-energy data that uses SK phases I through III to derive an upper bound on the supernova relic neutrinos (Hosaka *et al.*, 2006; Cravens *et al.*, 2008; K. Abe *et al.*, 2011). This analysis covers neutrino energies from 10 to 200 MeV; see Li and Beacom (2014) for a recent discussion of backgrounds in the low-energy range. The upper limit on supernova relic neutrinos was then converted into dark matter annihilation constraints and was originally presented by Olivares-Del Campo *et al.* (2018), Olivares-Del Campo, Palomares-Ruiz, and Pascoli (2018), and Olivares-Del Campo (2019). Recently SK phase-IV data have placed new constraints on the $\bar{\nu}_e$ flux in the 10 to 30 MeV energy range (Linyan, 2018). These observations improve over KamLAND constraints (Gando *et al.*, 2012) by a factor of between 3 and 10 in their overlapping energy range. Thus, these observations dominate the constraints for dark matter masses below ~ 20 MeV. Where they overlap, the Olivares *et al.* limits are not quite as strong as the SK- $\bar{\nu}_e$ limits that we have presented, because their background modeling could not use angular information that is not publicly available.
- (2) *Super-Kamiokande galactic dark matter search.*—The teal region in Fig. 2 labeled “SK” is from Frankiewicz (2015). This analysis uses muon-neutrino data in the energy range between 1 GeV and 10 TeV collected by SK over 5325.8 days. Since this analysis relies on angular information that is not public, it has not been rescaled to account for our choice of galactic halo parameters.
- (3) *IceCube-DeepCore galactic dark matter search.*—The IceCube limits are from Aartsen *et al.* (2016a) and use 329 days of IceCube data. These limits place constraints for masses between 25 GeV and 10 TeV. At the lowest masses, these limits include data from DeepCore, an array of more closely spaced inner strings in IceCube. In addition, we include a limit derived from 3 yr of data primarily using tracks to constrain Galactic Center emission (Aartsen *et al.*, 2017b). For display purposes, we join these two lines, choosing the best limit at each point, and show it in navy blue, simply labeled “IceCube.”
- (4) *IceCube-Bhattacharya et al.* is from the channel-by-channel unbinned likelihood analysis of Bhattacharya *et al.* (2019) of the High-Energy Starting Event data, including energy, angular, and topology information. They include both galactic and extragalactic constraints. Constraints that we derive (IceCube-HE) using only spectral information follow these limits quite closely at higher energies since the small sample size prevents angular information from contributing significantly.
- (5) *ANTARES dedicated galactic dark matter search.*—The light blue region, labeled ANTARES, is from a Galactic Center analysis of 9 yr of ANTARES muon-neutrino and antineutrino data (Adrian-Martinez *et al.*, 2015; Albert *et al.*, 2017a). This covers the dark matter mass range from 53 GeV to 100 TeV.
- (6) *Baikal dedicated galactic dark matter search (not shown).*—The Baikal underwater neutrino telescope (Belolaptikov *et al.*, 1997; Aynutdinov *et al.*, 2006) NT-200 is a water-Cherenkov detector deployed in Lake Baikal, Russia. It has an instrumented volume of approximately 100 kt and is composed of 192 optical modules arranged on eight strings, with a typical distance between strings of 21 m. The Baikal Collaboration performed an analysis looking for dark matter annihilation in the Galactic Center into neutrinos using data recorded between April 1998 and February 2003 (Avrorin *et al.*, 2016). This analysis claimed to place limits on the cross section at the 10^{-22} cm³ s⁻¹ level for a 1 TeV dark matter mass. We do not add this result to our constraint summary, because there are stronger results in this mass range, but we do show the projections of the next-generation detector at Lake Baikal, the Gigaton Volume Detector (GVD).
- (7) *Combined IceCube and ANTARES dedicated galactic dark matter search (not shown).*—Recently Albert *et al.* (2020) performed a combined analysis of the IceCube and ANTARES datasets that corresponds to approximately 1000 days of the former and 2000 of the latter. The combined result only marginally improves the previously published results, which we include in this review. The most notable point of this review is the consideration of underfluctuations when placing constraints on the data. In previous work by ANTARES, when the obtained data limit exceeded the mean sensitivity the reported result was the sensitivity of the analysis, while in the previous IceCube work underfluctuations were taken into account in the statistical limit and reported. Given the underfluctuation of data observed in the ANTARES dataset, the combined result is approximately a factor of 2 stronger in the ANTARES dominated region. We do not show the results of this analysis in our plot summary for two reasons: the analysis reports the experiment-overlapping dark matter parameter range only from 50 GeV to 1 TeV and does not report the $\nu\bar{\nu}$ channel that we study in this review.

Finally, Fig. 2 includes next-generation sensitivities that can be reached by future experiments. These are shown as dashed lines.

- (1) *Deep Underground Neutrino Experiment.*—The DUNE far detector will be a 46.4 kt liquid argon time projection chamber (TPC) (Acciarri *et al.*, 2015; Abi *et al.*, 2020a) constructed at the Sanford Underground Research Facility (SURF) in South Dakota. Its main advantage in detecting neutrinos from DM annihilation is its improved particle identification, using morphological reconstruction, with respect to Cherenkov detectors like Super-Kamiokande, ANTARES, and IceCube, which can be exploited to

make improved measurements of solar neutrinos (Capozzi *et al.*, 2019). Thus, a dedicated DUNE analysis utilizing the expected improved directional capability can prove effective in a search for galactic dark matter annihilation to neutrinos. We derive projected sensitivities for dark matter masses in the range from 100 MeV to 30 GeV and show them in Fig. 2 as dashed orange lines. The dominant background in this energy range is from atmospheric neutrinos. We use the predictions provided by Honda *et al.* (2015) at the Homestake Gold Mine at SURF, taking into account oscillations through Earth using the nuSQuIDS package (Argüelles, Salvado, and Weaver, 2014, 2015, 2020). In our analysis, we consider e - and τ -flavored charged-current interactions and compare the expected energy distribution; i.e., we do not take into account event-by-event directional information. We use a fractional charged lepton energy resolution of $2\% + 15\%/\sqrt{E/\text{GeV}}$ (Acciarri *et al.*, 2015) and assume the idealized condition of 100% efficiency. In our analysis, charged-current electron-neutrino interactions are assumed to deposit all their energy in the detector, while tau-neutrino charged-current interactions will deposit less visible energy due to the invisible neutrinos produced in the prompt τ decay. Since we expect that DUNE morphological identification will be able to single out muon-neutrino charged-current processes, we choose to remove them from the analysis, as they are the primary contributor to the atmospheric neutrino background. Limits are derived using a binned Poisson likelihood and a background-informed method, as described in Sec. III.A. We note that, due to liquid argon TPC's morphological reconstruction capabilities, a proper Galactic Center analysis including directionality would benefit from the inclusion of muon-neutrino charged-current interactions, and thus our projections are conservative.

- (2) *Hyper-Kamiokande*.—Building on SK's technology, a new water-Cherenkov detector with a fiducial mass of 187 kton called Hyper-Kamiokande (HK) will be built in Kamioka, Japan (Abe *et al.*, 2018). Owing to its larger size, this detector will be able to place stronger limits on the DM annihilation cross section to neutrinos than its predecessor (Olivares-Del Campo, Palomares-Ruiz, and Pascoli, 2018). In fact, Hyper-Kamiokande was estimated to reach $\sim 10^{-25} \text{ cm}^3 \text{ s}^{-1}$ for 1 GeV dark matter and $\sim 10^{-22} \text{ cm}^3 \text{ s}^{-1}$ at 10^4 GeV after 10 yr of data taking (Migenda, 2017). Furthermore, the possibility of doping both the SK and HK detectors with Gd will reduce the dominant background for low-energy analyses by a factor of 5 and, consequently, improve the constraints on DM annihilation (Horiuchi, Beacom, and Dwek, 2009; Laha and Beacom, 2014; Bell, Dolan, and Robles, 2020). Bell, Dolan, and Robles (2020) performed a detailed directional analysis of DM annihilation in the MW, including a Monte Carlo simulation of the atmospheric and diffuse supernova neutrino background as well as

the detector geometry. Figure 2 shows their equivalent results for 5 yr of run-time, which range from $\langle\sigma v\rangle \lesssim 10^{-25} \text{ cm}^2$ at $m_\chi = 16$ MeV to $\langle\sigma v\rangle \lesssim 4.3 \times 10^{-24} \text{ cm}^2$ at 50 GeV. For the p - and d -wave constraints in Sec. II.C, we derive our own projected sensitivities for 5 yr of data taking for DM masses in the 100 MeV to 30 GeV range, as the directional dependence does not allow the Bell *et al.* curve to be rescaled.

As in our DUNE analysis, we assume that the dominant background in this energy range is due to atmospheric neutrinos, where we use the predictions provided by Honda *et al.* (2015) at the Kamioka Mine and allow these neutrinos to oscillate through Earth using the nuSQuIDS package (Argüelles, Salvado, and Weaver, 2014, 2015). We consider e - and τ -flavored charged-current interactions only, without taking directionality into account. We make the same assumptions as our DUNE analysis regarding energy deposition while using an energy resolution of $1.5\% + 2\%/\sqrt{E/\text{GeV}}$ (Jiang *et al.*, 2019). We use total energy rather than lepton visible energy, which leads to a sensitivity overestimate of $\sim 40\%$ but simplifies the analysis. In principle, it is possible to record lepton and proton energy above the proton Cherenkov threshold; see Fechner *et al.* (2009). We follow the same statistical procedure as in the DUNE analysis and, like DUNE, the sensitivity strength derives primarily from the expected electron- and tau-neutrino signal. Taking advantage of this channel explains why our estimates are better than the ones presented by Migenda (2017); see Beacom and Candia (2004) for a discussion on “shower power.” We have checked to ensure that the corresponding s -wave results agree well with Bell *et al.* below ~ 1 GeV within their quoted uncertainties. However, owing to the incorporation of angular observables enabled by their dedicated simulation, their limits are better by a factor of ~ 2 above ~ 1 GeV. These projected sensitivities, especially at low energies, are subject to a $\sim 30\%$ uncertainty due to a combination of atmospheric background uncertainties and neutrino cross sections.

- (3) *Jiangmen Underground Neutrino Observatory* JUNO (An *et al.*, 2016) is a 20 kt unsegmented liquid scintillator detector under deployment in the Guangdong province of China. The detector has a muon tracker on top of it and is also surrounded by water. Both of these systems can be used to veto cosmic-ray muons by either tagging them in the muon tracker or detecting their Cherenkov light in water. Because of its large volume and good energy resolution (estimated to be $3\%/\sqrt{E/\text{MeV}}$) we expect that this experiment will have good sensitivity for neutrino-line searches. We estimate the sensitivity of JUNO to dark matter annihilation to neutrinos in the electron-antineutrino channel following the proposal given by Palomares-Ruiz and Pascoli (2008). We use background estimates derived for diffuse supernova background searches, as presented by An *et al.* (2016). Below 11 MeV, reactor

antineutrinos dominate the background. Between 11 and 40 MeV, the backgrounds are primarily neutral-current interactions from atmospheric neutrinos, with subdominant charged-current contributions. According to our projection, JUNO is expected to constrain the velocity-averaged annihilation cross section better than $10^{-25} \text{ cm}^3 \text{ s}^{-1}$ in the 10–40 MeV mass range. The estimate is shown in dark red in Fig. 2.

- (4) *The India-based Neutrino Observatory (INO; not shown)* The 50 kt magnetized Iron Calorimeter (ICAL) (Ahmed *et al.*, 2017; Indumathi, 2019) at the INO is a planned segmented *mille-feuille* of iron plates interleaved with resistive plate chambers (RPCs). The three modules will contain 151 iron leaves each, and a total of over 30 000 RPC units. A 1.5 T magnetic field will allow discrimination between muon neutrinos and antineutrinos. Following the successful completion of the mini-ICAL prototype, the INO underground laboratory and ICAL experiment are scheduled for construction at Pottipuram, in the Bodi West hills of the Theni District of Tamil Nadu, India. Khatun, Laha, and Agarwalla (2017) performed a forecast of the ICAL sensitivity to DM annihilation to neutrinos. The ability to discriminate between the ν and $\bar{\nu}$ events provides a factor of 2 to 3 boost in sensitivity, which, when rescaled to 5 yr, ranges from $\langle\sigma v\rangle \gtrsim 2 \times 10^{-24} \text{ cm}^3 \text{ s}^{-1}$ at $m_\chi = 2 \text{ GeV}$ to $10^{-23} \text{ cm}^3 \text{ s}^{-1}$ at 90 GeV.
- (5) *IceCube Upgrade*.—The IceCube Upgrade is an extension of the current IceCube-DeepCore array with seven closely packed strings. These new strings will be separated by approximately 20 m and each will contain 100 photomultiplier tubes spaced vertically by 3 m (Ishihara, 2019). Additionally, a number of calibration devices and sensors will be deployed to improve the modeling of the ice (Ishihara and Kiriki, 2019; Nagai and Ishihara, 2019). Baur (2019) performed a preliminary estimation of the IceCube Upgrade sensitivity. It is expected to be better than $10^{-24} \text{ cm}^3 \text{ s}^{-1}$ for a 10 GeV dark matter mass.
- (6) *IceCube Gen2*: The next-generation ice Cherenkov neutrino observatory in Antarctica is a substantial expansion to the current IceCube Neutrino Observatory aiming at enhancing the detector volume by a factor of 10 (Aartsen *et al.*, 2014b). This increased effective area is expected to provide a better sensitivity to resolve sources of high-energy cosmic neutrinos and identify components of cosmic neutrino flux. Dark matter annihilation limits from IceCube presented here should therefore scale by at least the increased sample size due to the larger effective area. We have recast the estimates of diffuse flux sensitivity given by Aartsen *et al.* (2019) to estimate the sensitivity to dark matter annihilation.
- (7) *The Baikal Gigaton Volume Detector*.—The Baikal GVD is a planned expansion to the existing NT-200 detector and is currently being deployed in Lake Baikal, Russia. The detector has recently reached an effective volume of $\sim 0.35 \text{ km}^3$ and has already seen first ν light (Avrorin *et al.*, 2019). The full array will contain 10 386 optical modules divided among 27 clusters of strings and is expected to have a final instrumented volume of around 1.5 km^3 . The sensitivity of GVD to galactic dark matter annihilation was estimated by Avrorin *et al.* (2015) and is shown as a dashed brown line labeled “GVD.”
- (8) *KM3Net*.—The km^3 -scale water-Cherenkov detector currently under construction in the Mediterranean Sea is designed to provide high-purity increased effective areas in the Southern Hemisphere. The larger effective area and improved angular resolution relative to ANTARES are expected to provide better constraints on galactic dark matter. Two separate sites are under construction for low- and high-energy regimes (Adrian-Martinez *et al.*, 2016). The high-energy site, called KM3NeT/ARCA, will consist of two detector array blocks located approximately 100 km offshore of Porto Palo di Capo Passero, Sicily, Italy (Aiello *et al.*, 2019). Each block is expected to have 115 strings with an average spacing of 90 m. The low-energy site, called KM3NeT/ORCA, consists of one array block and is under deployment approximately 40 km south of Toulon, France, close to the ANTARES site. The array is made out of 115 strings with an average horizontal spacing of 20 m. Each string contains 18 optical modules; in KM3NeT/ARCA they are spaced vertically by 36 m, while in KM3NeT/ORCA they are spaced 9 m apart. The horizontal spacing and number of strings are proportional to the effective volume of the experiment, while the vertical spacing is related to the energy threshold (Halzen, 2005). KM3NeT/ARCA’s science program is mainly oriented toward higher-energy astrophysical neutrino searches, while KM3NeT/ORCA will measure neutrino oscillations using atmospheric neutrinos. Assuming an E^{-2} democratic-flavor astrophysical neutrino flux with a normalization of $\sim 1.8 \times 10^{-8} \text{ GeV}^{-1} \text{ s}^{-1} \text{ cm}^{-1} \text{ sr}^{-1}$ and an exponential cutoff at 3 PeV, they expect to see 11 ν_μ ’s, 41 ν_e ’s, and 26 ν_τ ’s in 5 yr of KM3NeT/ARCA operation (Adrian-Martinez *et al.*, 2016). In Fig. 2 we show the KM3NeT/ARCA expected sensitivity to dark matter annihilation to neutrinos in 5 yr of data taking (Gozzini, 2019). Their sensitivity is within a factor of a few from the expected relic abundance cross section for dark matter masses around a TeV.
- (9) *The Pacific-Ocean Neutrino Experiment (P-ONE)*.—P-ONE is a newly proposed multicubic kilometer neutrino detector utilizing seawater as the Cherenkov medium (Agostini *et al.*, 2020). P-ONE would be deployed in the Cascadia Basin, off the coast of Vancouver Island in the Pacific Ocean, taking full advantage of the Ocean Network Canada infrastructure and expertise that is already in place. The main goal of the experiment is to explore the origin of the extraterrestrial neutrino flux. A pair of test strings, named STRAW (Bedard *et al.*, 2019), have already been successfully deployed and have collected water absorption data. The first phase of the detector, known as the Pacific Ocean Neutrino Explorer, involving ten strings is planned to be deployed in 2023. Each string is planned to be equipped with 20 photomultiplier

tubes. The full detector is expected to be complete by 2030 with 70 strings. Projected limits include backgrounds from atmospheric and diffuse astrophysical neutrinos and use the exposures shown by [Agostini *et al.* \(2020\)](#).

- (10) **TAMBO**: The Tau Air-Shower Mountain-Based Observatory is a proposed array of small water-Cherenkov tanks to be deployed in either the Colca Valley or the Cotahuasi Canyon in Peru ([Wissel *et al.*, 2019](#); [Romero-Wolf *et al.*, 2020](#)). These are two of the world’s four deepest valleys and their unique geometry allows for efficient detection of Earth-skimming PeV ν_τ . Most of the Colca Valley runs along a north-south corridor, although a smaller section of it has an east-west corridor. If deployed in the east-west corridor of the Colca Valley, the declination band covered is -15.5 ± 10 deg, while in the north-south corridor it would be -15.5 ± 50 deg. These two provide two extreme configurations in terms of its GC exposure, while a deployment in the Cotahuasi Canyon, which has an approximately diagonal corridor, would provide an intermediate exposure. TAMBO’s effective area is expected to be 10 times larger than IceCube ν_τ ([Aartsen *et al.*, 2013](#)) at a PeV and 30 times larger at 10 PeV. The use of the Earth-skimming technique is complementary to very-high-energy Earth-traversing neutrino searches ([Safa *et al.*, 2019](#)) and the fact that it relies on the Cherenkov effect, rather than the higher-energy threshold Askaryan effect, gives it unique potential to constrain dark matter in the tens of PeV mass range. Depending on the final geometry of TAMBO its sensitivity to dark matter ranges from 10^{-22} to 4×10^{-21} $\text{cm}^3 \text{s}^{-1}$ for a 1 PeV dark matter mass. Sensitivities shown here are recast from the diffuse flux sensitivity presented by ([Wissel *et al.*, 2019](#)). A similar detector has been proposed to be deployed in Hawaii ([Hou, 2014](#); [Sasaki, 2018, 2019](#)).
- (11) **CTA**.—The Cherenkov Telescope Array is a planned network of 99 air Cherenkov telescopes in the Southern Hemisphere and 19 in the Northern Hemisphere that will collectively provide full-sky coverage of the gamma-ray sky over an energy range of 20 GeV to 300 TeV ([Acharya *et al.*, 2018](#)). Several CTA prototypes have been built and some have already seen first light. The telescopes are projected to have an angular resolution down to 0.1 deg and a duty cycle of $\sim 15\%$. For high-mass dark matter annihilation into neutrinos, electroweak final-state radiation can also lead to the production of gamma rays, despite a completely “invisible” $\nu\bar{\nu}$ final state, and can thus be constrained by gamma-ray observations of the Galactic Center with CTA; see Sec. II for more details. The expected limits from CTA were computed by [Queiroz, Yaguna, and Weniger \(2016\)](#) and shown as a dashed silver line assuming 100 h of observation.

We note that the 10 MeV–1 GeV range can in principle be covered by future tonne-scale dark matter direct detection experiments such as DARWIN and ARGO ([McKee and Raj, 2018](#)). However, these are still in their planning phases, meaning that construction is still decades away, and long

($\gtrsim 10$ yr) exposure times are required to be competitive with HyperK. For this reason we do not show them here.

Figure 4 shows the extension of available constraints to larger masses above the “unitarity bound,” accessible for composite DM models ([Frigerio *et al.*, 2012](#)). These bounds are calculated by converting either the detected flux or the reported upper limits, from observatories sensitive to these mass range, into a conservative upper bound on the DM annihilation to neutrinos. The following experiments are sensitive to this regime.

- (1) **Auger**.—The Pierre Auger Observatory is a hybrid detector consisting of both an array of water-Cherenkov surface detectors and atmospheric fluorescence detectors. Located in Malargüe, Argentina ([Aab *et al.*, 2015b](#)) and operational since 2004, the Auger Collaboration has made a multitude of measurements of the highest energy cosmic rays. This includes measurements of the spectral distribution of cosmic rays beyond the Greisen-Zatsepin-Kuzmin (GZK) limit and anisotropy searches, as well as fits to their mass composition. Beyond the extensive cosmic-ray program, Auger is able to probe extremely-high-energy neutrinos by searching for showers developing deep in the atmosphere since showers induced by cosmic rays are likely to develop much earlier. Another possible detection channel is upgoing tau lepton showers, which are induced by Earth-skimming tau-neutrino interactions near Earth’s surface. In 2017, the Auger Collaboration reported a limit on the diffuse flux of high-energy neutrinos between 10^8 and 10^{11} GeV ([Zas, 2018](#)) that we use to set a background-agnostic bound on $\langle\sigma v\rangle$ for such energies (purple line in Fig. 4).
- (2) **IceCube-EHE**.—Beyond the astrophysical neutrino flux, IceCube performs searches for GZK neutrinos using a dedicated sample of events that deposit extremely high energies (EHE) in the detector. The most recent search used 9 yr of data and set limits on the GZK flux. We use these limits ([Aartsen *et al.*, 2018](#)) to derive an upper bound on the DM annihilation cross section to neutrinos between 10^7 and 10^{11} GeV, represented by a light brown line in Fig. 4.
- (3) **ANITA (not shown)**.—The Antarctic Impulsive Transient Antenna is an array of radio antennas attached to a helium balloon that flies for ~ 30 days at a time above Antarctica. The goal of this experiment is to measure the GZK cosmogenic neutrino flux by detecting radio showers emitted by extremely-high-energy neutrinos after interacting in the Antarctic ice ([Gorham *et al.*, 2009](#)). The ANITA Collaboration has successfully completed four such flights, setting the strongest limits on astrophysical neutrino fluxes above 10^{11} GeV, anomalies notwithstanding. We derive limits on dark matter annihilation to neutrinos by rescaling the reported upper limits from the fourth flight of ANITA ([Gorham *et al.*, 2019](#)). They extend up to $m_\chi = 10^{12}$ GeV but do not constrain $\langle\sigma v\rangle$ to be any smaller than 10^{-14} $\text{cm}^3 \text{s}^{-1}$, putting them outside of the range of Fig. 4.
- (4) **GRAND**: The Giant Radio Array for Neutrino Detection is a proposed large-scale observatory consisting of

200 000 radio antennas covering 200 000 km² near a mountain range in China. This experiment plans to use the surrounding mountains as a target for Earth-skimming tau neutrinos. After the neutrinos interact in the mountain, a tau lepton should be observed exiting the mountain and subsequently decaying in the atmosphere. The immense coverage will allow GRAND to probe GZK neutrino fluxes that are at least an order of magnitude below current limits (Alvarez-Muniz *et al.*, 2018). We convert their 3-yr sensitivity to the GZK neutrino flux between 10⁸ and 10¹¹ GeV into sensitivities on $\langle\sigma v\rangle$, which is shown as a dashed navy blue line in Fig. 4.

- (5) *RNO-G*: The Radio Neutrino Observatory in Greenland aims to measure the neutrino flux above 10¹⁶ eV (Aguilar *et al.*, 2019). The array of antennas to be deployed in the ice are designed to detect the Askaryan radio emission from extremely-high-energy neutrinos traversing Earth and the atmosphere. The design and deployment of RNO relies upon the experience and expertise obtained in successful deployment and operation of ARA and ARIANNA (Allison *et al.*, 2012; Barwick *et al.*, 2015). The plan is to deploy 35 stations such that each station consists of a surface array and a deep array. The surface array is going to be used for cosmic-ray detection, while the deep array, benefiting from a large effective volume, will detect neutrinos.
- (6) *BEACON (not shown)*.—Beamforming Elevated Array for Cosmic Neutrinos is another experiment proposed to search for the flux of very-high-energy neutrinos beyond 100 PeV. An array of antennas is installed at high elevations and presumes the use of a beam former radio array. The project is currently at the prototype stage, being tested at the White Mountain Research Station in California (Wissel *et al.*, 2020). The Cotahuasi Canyon, where TAMBO is deployed, has been considered as a potential site for BEACON. Given that the site of BEACON is yet to be confirmed, we have not projected the sensitivity for it in this review.
- (7) *POEMMA (not shown)*.—The Probe of Extreme Multi-Messenger Astrophysics is a proposed probe-class space mission to observe ultrahigh-energy cosmic rays and neutrinos above 20 PeV. Two satellites on near-equatorial orbits will observe fluorescence caused by showers in Earth’s atmosphere. When in stereo observation mode, POEMMA will effectively monitor 10¹³ metric tons of atmosphere (Anchordoqui *et al.*, 2020b; Olinto *et al.*, 2020). Preliminary diffuse neutrino flux sensitivity studies have projected as much as an order of magnitude improvement over existing limits at energies greater than 10¹⁰ GeV. We do not include POEMMA here, as neutrino sky coverage maps were not available at the time of this analysis.

A. Velocity-dependent annihilation

Figure 5 shows the corresponding limits for *p*-wave annihilation, and Fig. 6 provides limits on *d*-wave annihilation. In these cases, we follow the procedures outlined in

Sec. II.C to reweight the astrophysical portion of the flux prediction [Eqs. (1) and (9)] to account for the dark matter velocity dispersion. We do this for all-sky searches since analyses where the angular distribution of the neutrinos has been taken into account are not easily rescaled when considering the velocity distribution of DM particles within the halo. Similarly, all the constraints taken from the literature are rescaled using our choice of halo parameters (see Table I for the halo parameters and *J* factor for the different analyses in the literature). The limits on $\langle\sigma v\rangle$ are much weaker for *p*- and *d*-wave processes due to the strong velocity suppression. In contrast to the *s*-wave case, where the smallest halos tend to dominate the expected signal, velocity-suppressed annihilation is strongest in the largest DM halos, where dispersion velocities are higher. These limits are thus insensitive to the value of the minimum halo mass M_{\min} . However, the constraints from annihilation in the Milky Way halo remain dominant over the extragalactic contribution.

B. Dark matter halo uncertainties

As previously mentioned, a major source of uncertainty comes from the spatial dark matter distribution, because of the n_{χ}^2 dependence in the annihilation signal. For galactic constraints, this is mainly reflected by uncertainties in the Milky Way dark matter distribution. For extragalactic constraints, we focus on the shape of the halo mass function and the minimum dark matter mass, which determines how far down extrapolations of the HMF must go to account for the total DM contribution.

Milky Way halo shape parameters: To quantify the effect of the uncertainty on the MW halo shape parameters, we use the code provided by Benito, Cuoco, and Iocco (2019), which computes the log-likelihood as a function of the halo shape parameters $\{\rho_0, r_s, R_0, \gamma\}$, given observed stellar kinematics data. We profile over the 4 degrees of freedom, modifying the code to account for GRAVITY measurements of R_0 , and obtain 68% and 95% C.L. ranges on the *J* factors that we propagate to a range on $\langle\sigma v\rangle$ for the Borexino, SK, and IceCube analyses. These are shown as dark and light bands, respectively, in Fig. 7.

Halo mass function uncertainties.—The largest contributions to uncertainties in the cosmological limits come from (1) the choice of HMF parametrization, and (2) the choice of minimum halo mass M_{\min} . In our analyses we have employed the simulation-driven HMF fit by Watson *et al.* (2013). Figure 8 shows the boost factor $G(z)$ defined in Eq. (9) for four different parametrizations from the literature: the analytic Press and Schechter formalism (Press and Schechter, 1974; Bond *et al.*, 1991), Sheth and Tormen (Sheth and Tormen, 1999; Sheth, Mo, and Tormen, 2001), and Tinker *et al.* (2008). The width of the bands comes from varying the minimum halo mass from 10⁻³ M_{\odot} to 10⁻⁹ M_{\odot} . The band labeled “extragalactic” in Fig. 7 shows how this range propagates through to the cross-section constraints. Since there is no way of statistically quantifying the error on the HMF and minimum halo mass, we choose the most conservative scenario $M_{\min} = 10^{-3}M_{\odot}$ for our choice of HMF, corresponding to the solid magenta line in Fig. 7.

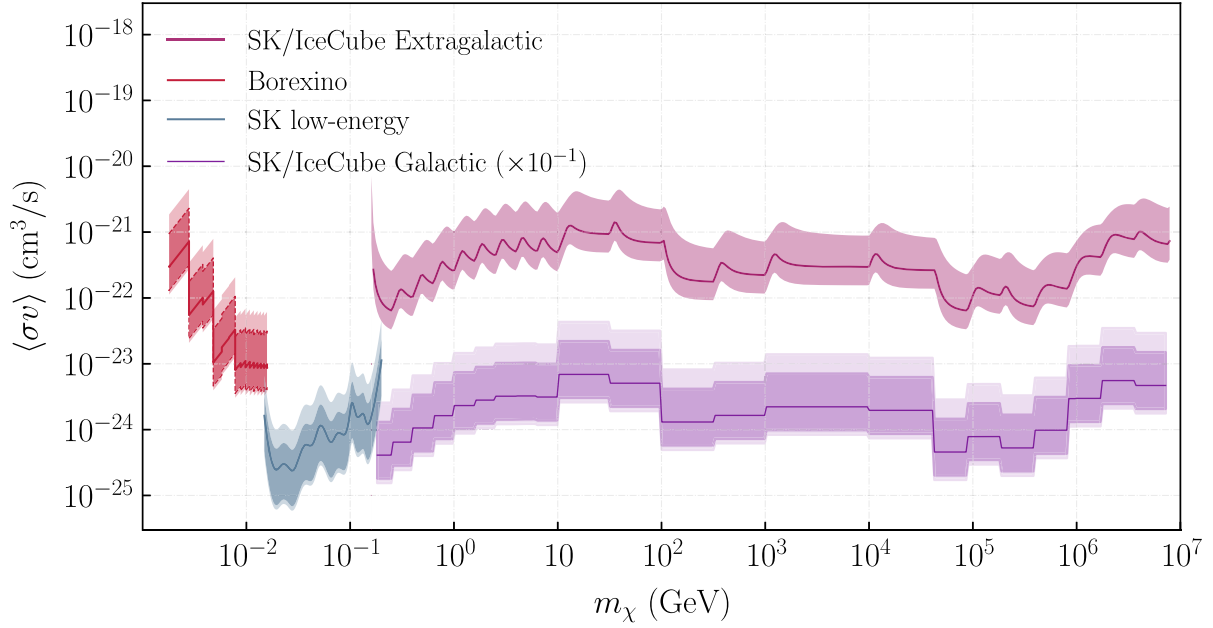


FIG. 7. Uncertainties on the s -wave annihilation cross section for a subset of our results. The solid lines correspond to the limits discussed in Sec. IV. For all galactic limits, namely, Borexino (red, leftmost), Super-Kamiokande low energy (gray, second region from left), and Super-Kamiokande and IceCube (lower, rightmost), the 68% (dark bands) and 95% (light bands) uncertainties arise from the allowed variation on the dark matter distribution in the Milky Way assuming a generalized NFW profile. The width of the uncertainty band for the extragalactic limits (upper, rightmost), obtained from a comparison to the unfolded neutrino flux from IceCube and Super-Kamiokande, is dominated by the choice of the minimum halo mass M_{\min} , although it includes the uncertainty in the choice of HMF dn/dM ; see Fig. 8. For our nominal choice of HMF, we choose the value of M_{\min} that yields the weakest constraint.

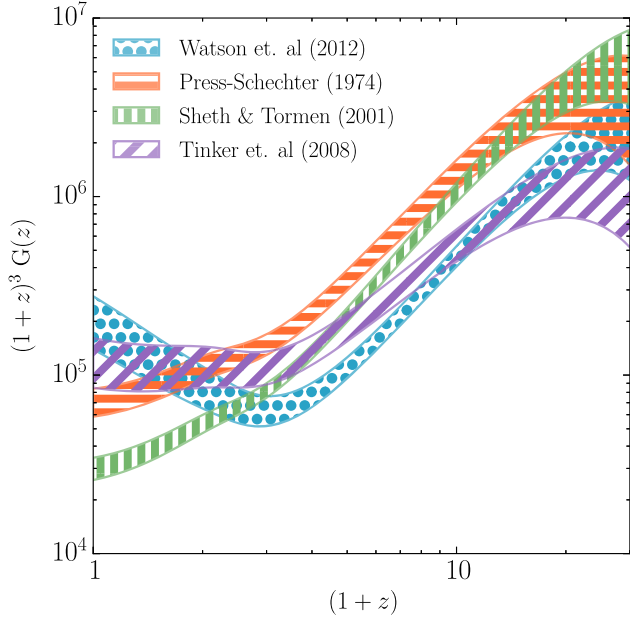


FIG. 8. Halo boost factor $G(z)$ as a function of redshift for several parametrizations of the HMF dn/dM . Our extragalactic constraints are from Watson *et al.* (2013). The bands represent varying choices of minimum halo mass, from $10^{-3}M_\odot$ to $10^{-9}M_\odot$. Figure 7 shows the effect of choosing a different parametrization on the limits.

V. DISCUSSION AND CONCLUSIONS

We have presented a comprehensive set of limits on dark matter annihilation directly to neutrino-antineutrino pairs for a DM mass range from 10^{-3} to 10^{12} GeV. There is uninterrupted coverage of this entire range by the multitude of neutrino detectors that have been in operation over the past decade. The strongest limits come from dedicated analyses that include direction and energy information, such as those performed by Super-Kamiokande (Frankiewicz, 2015, 2018), IceCube (Aartsen *et al.*, 2016a), and ANTARES (Adrian-Martinez *et al.*, 2016). Such analyses become difficult to accurately recast, as the event information and detector effective area and response are not typically made publicly available.

Because the DM density is a fixed constraint, the annihilation rate to neutrinos scales as m_χ^{-2} . A feature of the constraints presented here is that they remain approximately flat, rising only 2 orders of magnitude from $\langle\sigma v\rangle \lesssim 10^{-24}$ to 10^{-22} $\text{cm}^3 \text{s}^{-1}$ across 9 decades in energy. Above this range, sensitivity drops off with $\sim m_\chi^2$ since the neutrino cross section grows only logarithmically in this regime. We attribute the flattening to two main features, which highlight the unique promise of neutrino astronomy: (1) the neutrino-nucleus cross section, which determines the detection efficiency, grows strongly with center-of-mass energy until approximately $E_\nu = 10^6$ GeV, and (2) neutrino detectors built for high-energy observations must necessarily be larger to compensate for the lower expected flux from extragalactic sources, and the larger size of the detectable Cherenkov cascades caused by

neutrino interactions. At energies above $\sim 10^{10}$ GeV, neutrinos become the only probe of high-energy extragalactic processes.

For s -channel annihilation, next-generation experiments will finally venture below the expected thermal relic abundance for 10 MeV masses. In fact, our analysis of the recent SK phase-IV data (Linyan, 2018) is within a factor of a few of the relic abundance expected value. Similarly, with the realization of a cubic kilometer detector in the Northern Hemisphere, the sensitivity in the TeV energy range gets close to the thermal relic expectations. Beyond the expected thermal relic cross section there are some intriguing hints for dark matter that could be tested with neutrinos; we mention a few here.

The EDGES Collaboration recently reported an abnormally low-temperature absorption feature in the 21 cm global spectrum at a redshift of $z \sim 17$ (Bowman *et al.*, 2018), although the interpretation of this result has been questioned in a number of studies (Bradley *et al.*, 2019). If the observation does hold up to scrutiny and replication, it would be an indication of physics beyond the standard cosmological model. A suggested explanation is excess gas cooling by millicharged dark matter (Barkana, 2018; Klop and Ando, 2018; Muñoz and Loeb, 2018); see also Berlin *et al.* (2018). In such scenarios, a neutrino line is expected in the 10 MeV range (Klop and Ando, 2018). This model requires 2% of the DM to annihilate to muon and tau neutrinos, with a cross section around $10^{-25} \text{ cm}^3 \text{ s}^{-1}$. As indicated in Fig. 2, this parameter space is rapidly closing.

Goodenough and Hooper (2009) noted an excess of gamma rays seen by the spaceborne Fermi-LAT instrument in the direction of the Galactic Center in an energy range of 3–10 GeV. Despite considerable debate, this signal remains consistent with what is expected from DM annihilation (Leane and Slatyer, 2019); e.g., it can be well explained by dark matter annihilation into $b\bar{b}$ with a mass of ~ 30 GeV and an annihilation cross section of the order of $10^{-26} \text{ cm}^3 \text{ s}^{-1}$ (Hooper and Goodenough, 2011; Calore, Cholis, and Weniger, 2015; Daylan *et al.*, 2016). Recent analyses of the AMS-02 cosmic-ray data (Aguilar *et al.*, 2016) found hints of an excess in cosmic-ray antiprotons that can also be explained by ~ 30 GeV WIMPs annihilating to W^+W^- or b quark pairs with a similar cross section (Cuoco, Krämer, and Korsmeier, 2017). The detection of a neutrino signal complementary with what is seen in the GC would be a powerful indication of new physics processes at work. Caution is warranted, as the antiproton excess could well be attributed to systematic uncertainties in cosmic-ray propagation (Boudaud *et al.*, 2020) or a combination of propagation uncertainties, nuclear cross-section uncertainties, and correlations in instrumental systematics (Heisig, Korsmeier, and Winkler, 2020).

Additionally, growing statistics for different channels for observation of high-energy neutrinos in IceCube (Aartsen *et al.*, 2016b; Schneider, 2019) hints toward a more complex spectral scenario and possible features in the flux of cosmic neutrinos. Analysis of the contained neutrino events at lower energies (~ 10 TeV) has revealed a flux that is an order of magnitude higher than the flux at PeV energies (Aartsen *et al.*,

2015a). This is usually referred to as the “low-energy excess” in IceCube data. The origin of these neutrinos are thought to be different from the bulk of neutrino emission at PeV energies; see Murase, Guetta, and Ahlers (2016) for more discussion. Models assuming DM annihilation (or decay) into high-energy neutrinos have been proposed to describe the low-energy excess (Chianese, Miele, and Morisi, 2017; Bhattacharya *et al.*, 2019) [see also Sui and Bhupal Dev (2018)], and they show a slight preference for a potential component from TeV dark matter. However, such an interpretation could be in tension with gamma-ray observations (Chianese *et al.*, 2018). At the moment, elucidating the origin of the high-energy neutrino excess will require correlated observations with gamma rays and novel analysis techniques; see Dekker, Chianese, and Ando (2019).

The ANITA balloon-borne experiment has recently reported on two events originating from 30° or more below the horizon (Gorham *et al.*, 2016, 2018), with energies in excess of 500 PeV. This is unexpected, as Earth should be opaque to neutrinos at these energies. These are not consistent with either a diffuse primary neutrino flux or a point source hypothesis, as the secondary interaction products would have been observed at IceCube (Romero-Wolf *et al.*, 2019; Safa *et al.*, 2019; Aartsen *et al.*, 2020). Systematic effects regarding irregularities in the Antarctic surface ice have been proposed (Shoemaker *et al.*, 2019). However, dark matter that decays (Cline, Gross, and Xue, 2019; Hooper *et al.*, 2019) or annihilates (Esmaili and Farzan, 2019) to neutrinos or boosted DM could also explain such a signal, although more data are still required to test such hypotheses (Anchordoqui *et al.*, 2020a; Dudas *et al.*, 2020).

We hope for further surprises and point out the room for improvement with dedicated analyses; e.g., our DUNE and HK estimations do not yet use directional information. Likewise, high-energy neutrino observatories are expected to improve their angular and energy resolutions in the next generation and a combination of their datasets would improve over our projected sensitivities.

The annihilation of dark matter to neutrino pairs is the most invisible channel: the constraints that we have provided here are thus closing the window on dark matter annihilation into standard model products, and are therefore rapidly narrowing down the available parameter space where WIMP-like dark matter may still be hiding.

ACKNOWLEDGMENTS

We would like to thank John Beacom, Mauricio Bustamante, Claire Guépin, Francis Halzen, Julian Heeck, Matheus Hostert, Teppei Katori, Gordan Krnjaic, Elisa Resconi, Andrés Romero-Wolf, Carsten Rott, and Sergio Palomares-Ruiz for useful discussions. We thank the anonymous referees for excellent suggestions and comments. We are grateful to have had the chance to work with our friend and colleague A. O.-D.-C. and wish him the best success in his future endeavours. C. A. A. and A. D. are supported by NSF Grant No. PHY-1912764. A. K. acknowledges support from the IGC Postdoctoral Fellowship. I. S. is supported by NSF Grants No. PLR-1600823 and No. OPP-1600823. A. C. V. is supported by the Arthur B. McDonald Canadian Astroparticle

Physics Research Institute, with equipment funded by the Canada Foundation for Innovation and the Ontario Ministry of Economic Development, Job Creation and Trade (MEDJCT). Research at Perimeter Institute is supported by the Government of Canada through the Department of Innovation, Science and Economic Development, and by the Province of Ontario through MEDJCT. C. A. A is supported by the Faculty of Arts and Sciences of Harvard University.

REFERENCES

- Aab, A., *et al.* (Pierre Auger Collaboration), 2015a, *Phys. Rev. D* **91**, 092008.
- Aab, A., *et al.* (Pierre Auger Collaboration), 2015b, *Nucl. Instrum. Methods Phys. Res., Sect. A* **798**, 172.
- Aalbers, J., *et al.* (DARWIN Collaboration), 2016, *J. Cosmol. Astropart. Phys.* **11**, 017.
- Aartsen, M. G., *et al.* (IceCube Collaboration), 2013, *Science* **342**, 1242856.
- Aartsen, M. G., *et al.* (IceCube Collaboration), 2014a, *J. Instrum.* **9**, P03009.
- Aartsen, M. G., *et al.* (IceCube Collaboration), 2014b, *arXiv:1412.5106*.
- Aartsen, M. G., *et al.* (IceCube Collaboration), 2014c, *Phys. Rev. Lett.* **113**, 101101.
- Aartsen, M. G., *et al.* (IceCube Collaboration), 2015a, *Phys. Rev. D* **91**, 022001. Aartsen, M. G., *et al.* (IceCube Collaboration), 2015b, *Phys. Rev. D* **91**, 122004.
- Aartsen, M. G., *et al.* (IceCube Collaboration), 2016a, *Eur. Phys. J. C* **76**, 531. Aartsen, M. G., *et al.* (IceCube Collaboration), 2016b, *Astrophys. J.* **833**, 3.
- Aartsen, M. G., *et al.* (IceCube Collaboration), 2017a, *Eur. Phys. J. C* **77**, 692.
- Aartsen, M. G., *et al.* (IceCube Collaboration), 2017b, *Eur. Phys. J. C* **77**, 627.
- Aartsen, M. G., *et al.* (IceCube Collaboration), 2017c, *J. Instrum.* **12**, P03012.
- Aartsen, M. G., *et al.* (IceCube Collaboration), 2018, *Phys. Rev. D* **98**, 062003.
- Aartsen, M. G., *et al.* (IceCube Collaboration), 2019, *arXiv:1911.02561*.
- Aartsen, M. G., *et al.* (IceCube Collaboration), 2020, *arXiv:2001.01737*.
- Abbasi, R., *et al.* (IceCube Collaboration), 2020, *arXiv:2011.03545*.
- Abe, K., *et al.* (Hyper-Kamiokande Collaboration), 2018, *arXiv:1805.04163*.
- Abe, K., *et al.* (Super-Kamiokande Collaboration), 2011, *Phys. Rev. D* **83**, 052010.
- Abe, K., *et al.* (Super-Kamiokande Collaboration), 2020, *arXiv:2005.05109*.
- Abe, S., *et al.* (KamLAND Collaboration), 2011, *Phys. Rev. C* **84**, 035804.
- Abi, B., *et al.* (DUNE Collaboration), 2020a, *J. Instrum.* **15**, T08008.
- Abi, B., *et al.* (DUNE Collaboration), 2020b, *arXiv:2002.03005*.
- Abrahamyan, S., *et al.* (APEX Collaboration), 2011, *Phys. Rev. Lett.* **107**, 191804.
- Abuter, R., *et al.* (GRAVITY Collaboration), 2018, *Astron. Astrophys.* **615**, L15.
- Acciarri, R., *et al.* (DUNE Collaboration), 2015, *arXiv:1512.06148*.
- Acciarri, R., *et al.* (MicroBooNE Collaboration), 2017, *J. Instrum.* **12**, P02017.
- Acciarri, R., *et al.* (MicroBooNE Collaboration), 2018, *Eur. Phys. J. C* **78**, 82.
- Acharya, B. S., *et al.* (CTA Consortium), 2018, *arXiv:1709.07997*.
- Adams, C., *et al.* (MicroBooNE Collaboration), 2019, *Phys. Rev. D* **99**, 092001.
- Adrian-Martinez, S., *et al.* (ANTARES Collaboration), 2015, *J. Cosmol. Astropart. Phys.* **10**, 068.
- Adrian-Martinez, S., *et al.* (KM3Net Collaboration), 2016, *J. Phys. G* **43**, 084001.
- Aghanim, N., *et al.* (Planck Collaboration), 2018, *arXiv:1807.06209*.
- Agostini, M., *et al.*, 2020, *arXiv:2005.09493*.
- Agostini, M., *et al.* (Borexino Collaboration), 2018, *Nature (London)* **562**, 505.
- Agostini, M., *et al.* (Borexino Collaboration), 2019, *arXiv:1909.02422*.
- Aguilar, J., *et al.*, 2019, *arXiv:1907.12526*.
- Aguilar, M., *et al.* (AMS Collaboration), 2016, *Phys. Rev. Lett.* **117**, 091103.
- Aguilar-Arevalo, A. A., *et al.* (MiniBooNE Collaboration), 2017, *Phys. Rev. Lett.* **118**, 221803.
- Ahmad, Q., *et al.* (SNO Collaboration), 2001, *Phys. Rev. Lett.* **87**, 071301.
- Ahmed, S., *et al.* (ICAL Collaboration), 2017, *Pramana* **88**, 79.
- Aiello, S., *et al.* (KM3NeT Collaboration), 2019, *Astropart. Phys.* **111**, 100.
- Akimov, D., *et al.* (COHERENT Collaboration), 2017, *Science* **357**, 1123.
- Albert, A., *et al.*, 2017a, *Phys. Lett. B* **769**, 249; **796**, 253(E) (2019).
- Albert, A., *et al.* (Fermi-LAT and DES Collaborations), 2017b, *Astrophys. J.* **834**, 110.
- Albert, A., *et al.* (ANTARES and IceCube Collaborations), 2020, *arXiv:2003.06614*.
- Aliaga, L., *et al.* (MINERvA Collaboration), 2014, *Nucl. Instrum. Methods Phys. Res., Sect. A* **743**, 130.
- Alikhanov, I., 2016, *Phys. Lett. B* **756**, 247.
- Ali-Mohammadzadeh, B., *et al.*, 2020, *arXiv:2006.05261*.
- Alimonti, G., *et al.* (Borexino Collaboration), 2002, *Astropart. Phys.* **16**, 205.
- Alimonti, G., *et al.* (Borexino Collaboration), 2009, *Nucl. Instrum. Methods Phys. Res., Sect. A* **600**, 568.
- Allison, P., *et al.* (ARA Collaboration), 2012, *Astropart. Phys.* **35**, 457.
- Allison, P., *et al.* (ARA Collaboration), 2019, *arXiv:1912.00987*.
- Alvarez-Muniz, J., *et al.* (GRAND Collaboration), 2018, *arXiv:1810.09994*.
- Alvey, J. B. G., and M. Fairbairn, 2019, *arXiv:1902.01450*.
- An, F., *et al.* (JUNO Collaboration), 2016, *J. Phys. G* **43**, 030401.
- Anchordoqui, L., *et al.*, 2020a, *Proc. Sci., ICRC2019*, 884 [*arXiv:1907.06308*].
- Anchordoqui, L. A., *et al.*, 2020b, *Phys. Rev. D* **101**, 023012.
- Anderson, M., *et al.* (SNO+ Collaboration), 2019, *Phys. Rev. D* **99**, 032008.
- Andringa, S., *et al.* (SNO+ Collaboration), 2016, *Adv. High Energy Phys.* **6194250**.
- Anker, A., *et al.*, 2020, *arXiv:2004.09841*.
- Ankowski, A. M., 2016, *arXiv:1601.06169*.
- Arcadi, G., M. Dutra, P. Ghosh, M. Lindner, Y. Mambrini, M. Pierre, S. Profumo, and F. S. Queiroz, 2018, *Eur. Phys. J. C* **78**, 203.
- Argüelles, C. A., M. Hostert, and Y.-D. Tsai, 2018, *arXiv:1812.08768*.
- Argüelles, C. A., A. Kheirandish, and A. C. Vincent, 2017, *Phys. Rev. Lett.* **119**, 201801.
- Argüelles, C. A., J. Salvado, and C. N. Weaver, 2014, *arXiv:1412.3832*.

- Argüelles, C. A., J. Salvado, and C. N. Weaver, 2015, computer code nuSQuIDS, <https://github.com/Arguelles/nuSQuIDS>.
- Argüelles, C. A., J. Salvado, and C. N. Weaver, 2020, *Comput. Phys. Commun.* **255**, 107405.
- Argüelles, C. A., A. Schneider, and T. Yuan, 2019, *J. High Energy Phys.* **06**, 030.
- Argüelles, C. A., *et al.*, 2019, [arXiv:1907.08311](https://arxiv.org/abs/1907.08311).
- Arpessella, C., *et al.* (Borexino Collaboration), 2008, *Phys. Rev. Lett.* **101**, 091302.
- Askar'yan, G., 1962, *Sov. Phys. JETP* **14**, 441.
- Aurisano, A., A. Radovic, D. Rocco, A. Himmel, M. Messier, E. Niner, G. Pawloski, F. Psihas, A. Sousa, and P. Vahle, 2016, *J. Instrum.* **11**, P09001.
- Avrorin, A. D., *et al.*, 2015, *JETP Lett.* **101**, 289.
- Avrorin, A. D., *et al.* (Baikal Collaboration), 2016, *Astropart. Phys.* **81**, 12.
- Avrorin, A. D., *et al.* (Baikal-GVD Collaboration), 2019, [arXiv:1908.05450](https://arxiv.org/abs/1908.05450).
- Aynutdinov, V. M., *et al.*, 2006, *Phys. At. Nucl.* **69**, 1914.
- Backhouse, C., and R. Patterson, 2015, *Nucl. Instrum. Methods Phys. Res., Sect. A* **778**, 31.
- Ballett, P., M. Hostert, and S. Pascoli, 2019a, [arXiv:1903.07589](https://arxiv.org/abs/1903.07589).
- Ballett, P., M. Hostert, and S. Pascoli, 2019b, *Phys. Rev. D* **99**, 091701.
- Ballett, P., S. Pascoli, and M. Ross-Lonergan, 2019, *Phys. Rev. D* **99**, 071701.
- Barenboim, G., P. B. Denton, and I. M. Oldengott, 2019, *Phys. Rev. D* **99**, 083515.
- Barkana, R., 2018, *Nature (London)* **555**, 71.
- Barlow, R. J., and C. Beeston, 1993, *Comput. Phys. Commun.* **77**, 219.
- Barwick, S., *et al.* (ARIANNA Collaboration), 2015, *Astropart. Phys.* **70**, 12.
- Bauer, C. W., N. L. Rodd, and B. R. Webber, 2020, [arXiv:2007.15001](https://arxiv.org/abs/2007.15001).
- Baumholzer, S., V. Brdar, P. Schwaller, and A. Segner, 2019, [arXiv:1912.08215](https://arxiv.org/abs/1912.08215).
- Baur, S. (IceCube Collaboration), 2019, [arXiv:1908.08236](https://arxiv.org/abs/1908.08236).
- Beacom, J. F., N. F. Bell, and G. D. Mack, 2007, *Phys. Rev. Lett.* **99**, 231301.
- Beacom, J. F., and J. Candia, 2004, *J. Cosmol. Astropart. Phys.* **11**, 009.
- Beacom, J. F., and M. R. Vagins, 2004, *Phys. Rev. Lett.* **93**, 171101.
- Bedard, J., *et al.* (STRAW Collaboration), 2019, [arXiv:1810.13265](https://arxiv.org/abs/1810.13265).
- Bell, N. F., Y. Cai, J. B. Dent, R. K. Leane, and T. J. Weiler, 2017, *Phys. Rev. D* **96**, 023011.
- Bell, N. F., M. J. Dolan, and S. Robles, 2020, [arXiv:2005.01950](https://arxiv.org/abs/2005.01950).
- Bellini, G., *et al.* (Borexino Collaboration), 2010, *Phys. Lett. B* **687**, 299.
- Bellini, G., *et al.* (Borexino Collaboration), 2011, *Phys. Lett. B* **696**, 191.
- Belolaptikov, I. A., *et al.* (BAIKAL Collaboration), 1997, *Astropart. Phys.* **7**, 263.
- Benito, M., N. Bernal, N. Bozorgnia, F. Calore, and F. Iocco, 2017, *J. Cosmol. Astropart. Phys.* **02**, 007; **06**, E01 (2018).
- Benito, M., A. Cuoco, and F. Iocco, 2019, *J. Cosmol. Astropart. Phys.* **03**, 033.
- Berestetskii, V. B., L. P. Pitaevskii, and E. M. Lifshitz, 1974, *Relativistic Quantum Theory, Part I*, Course of Theoretical Physics Vol. 4 (Pergamon Press, New York).
- Berlin, A., D. Hooper, G. Krnjaic, and S. D. McDermott, 2018, *Phys. Rev. Lett.* **121**, 011102.
- Bertone, G., and D. Hooper, 2018, *Rev. Mod. Phys.* **90**, 045002.
- Bertuzzo, E., S. Jana, P. A. N. Machado, and R. Zukanovich Funchal, 2018, *Phys. Rev. Lett.* **121**, 241801.
- Besson, D., N. Doolin, M. Stockham, and I. Kravchenko, 2012, *Cryosphere Discuss.* **6**, 4695.
- Bhattacharya, A., A. Esmaili, S. Palomares-Ruiz, and I. Sarcevic, 2019, *J. Cosmol. Astropart. Phys.* **05**, 051.
- Blanco, C., M. Escudero, D. Hooper, and S. J. Witte, 2019, [arXiv:1907.05893](https://arxiv.org/abs/1907.05893).
- Blennow, M., E. Fernandez-Martinez, A. O.-D. Campo, S. Pascoli, S. Rosauero-Alcaraz, and A. V. Titov, 2019, [arXiv:1903.00006](https://arxiv.org/abs/1903.00006).
- Boddy, K. K., J. Kumar, and L. E. Strigari, 2018, [arXiv:1805.08379](https://arxiv.org/abs/1805.08379).
- Boehm, C., M. J. Dolan, and C. McCabe, 2012, *J. Cosmol. Astropart. Phys.* **12**, 027.
- Boehm, C., M. J. Dolan, and C. McCabe, 2013, *J. Cosmol. Astropart. Phys.* **08**, 041.
- Boehm, C., Y. Farzan, T. Hambye, S. Palomares-Ruiz, and S. Pascoli, 2008, *Phys. Rev. D* **77**, 043516.
- Bohm, G., and G. Zech, 2014, *Nucl. Instrum. Methods Phys. Res., Sect. A* **748**, 1.
- Bond, J. R., S. Cole, G. Efstathiou, and N. Kaiser, 1991, *Astrophys. J.* **379**, 440.
- Boudaud, M., Y. Génolini, L. Derome, J. Lavalle, D. Maurin, P. Salati, and P. D. Serpico, 2020, *Phys. Rev. Research* **2**, 023022.
- Bowman, J. D., A. E. E. Rogers, R. A. Monsalve, T. J. Mozdzen, and N. Mahesh, 2018, *Nature (London)* **555**, 67.
- Bradley, R. F., K. Tauscher, D. Rapetti, and J. O. Burns, 2019, *Astrophys. J.* **874**, 153.
- Calore, F., I. Cholis, and C. Weniger, 2015, *J. Cosmol. Astropart. Phys.* **03**, 038.
- Capozzi, F., S. W. Li, G. Zhu, and J. F. Beacom, 2019, *Phys. Rev. Lett.* **123**, 131803.
- Capozzi, F., I. M. Shoemaker, and L. Vecchi, 2017, *J. Cosmol. Astropart. Phys.* **07**, 021.
- Capozzi, F., I. M. Shoemaker, and L. Vecchi, 2018, *J. Cosmol. Astropart. Phys.* **07**, 004.
- Cappiello, C., and J. F. Beacom, 2019, *Phys. Rev. D* **100**, 103011.
- Carena, M., A. Daleo, B. A. Dobrescu, and T. M. P. Tait, 2004, *Phys. Rev. D* **70**, 093009.
- Cavanna, F., A. Ereditato, and B. Fleming, 2018, *Nucl. Instrum. Methods Phys. Res., Sect. A* **907**, 1.
- Cherry, J. F., A. Friedland, and I. M. Shoemaker, 2016, [arXiv:1605.06506](https://arxiv.org/abs/1605.06506).
- Chianese, M., D. F. G. Fiorillo, G. Miele, S. Morisi, and O. Pisanti, 2019, *J. Cosmol. Astropart. Phys.* **11**, 046.
- Chianese, M., G. Miele, and S. Morisi, 2017, *Phys. Lett. B* **773**, 591.
- Chianese, M., G. Miele, S. Morisi, and E. Peinado, 2018, *J. Cosmol. Astropart. Phys.* **12**, 016.
- Chirkin, D., 2013, [arXiv:1304.0735](https://arxiv.org/abs/1304.0735).
- Choi, K.-Y., J. Kim, and C. Rott, 2019, *Phys. Rev. D* **99**, 083018.
- Cline, J. M., C. Gross, and W. Xue, 2019, *Phys. Rev. D* **100**, 015031.
- Cohen, T., K. Murase, N. L. Rodd, B. R. Safdi, and Y. Soreq, 2017, *Phys. Rev. Lett.* **119**, 021102.
- Conrad, J., A. de Gouvea, S. Shalgar, and J. Spitz, 2010, *Phys. Rev. D* **82**, 093012.
- Cornell, J. M., S. Profumo, and W. Shepherd, 2013, *Phys. Rev. D* **88**, 015027.
- Cousins, R. D., and V. L. Highland, 1992, *Nucl. Instrum. Methods Phys. Res., Sect. A* **320**, 331.
- Cowen, D. F. (IceCube Collaboration), 2007, *J. Phys. Conf. Ser.* **60**, 227.
- Cravens, J. P., *et al.* (Super-Kamiokande Collaboration), 2008, *Phys. Rev. D* **78**, 032002.

- Cuoco, A., M. Krämer, and M. Korsmeier, 2017, *Phys. Rev. Lett.* **118**, 191102.
- Davis, J. H., and J. Silk, 2015, [arXiv:1505.01843](https://arxiv.org/abs/1505.01843).
- Daylan, T., D. P. Finkbeiner, D. Hooper, T. Linden, S. K. N. Portillo, N. L. Rodd, and T. R. Slatyer, 2016, *Phys. Dark Universe* **12**, 1.
- Dekker, A., M. Chianese, and S. Ando, 2019, [arXiv:1910.12917](https://arxiv.org/abs/1910.12917).
- Diamanti, R., L. Lopez-Honorez, O. Mena, S. Palomares-Ruiz, and A. C. Vincent, 2014, *J. Cosmol. Astropart. Phys.* **02**, 017.
- Diaz, A., C. Argüelles, G. Collin, J. Conrad, and M. Shaevitz, 2019, [arXiv:1906.00045](https://arxiv.org/abs/1906.00045).
- Dudas, E., L. Heurtier, Y. Mambrini, K. A. Olive, and M. Pierre, 2020, [arXiv:2003.02846](https://arxiv.org/abs/2003.02846).
- El Aisati, C., 2018, Ph.D. thesis (Free University of Brussels).
- El Aisati, C., C. Garcia-Cely, T. Hambye, and L. Vanderheyden, 2017, *J. Cosmol. Astropart. Phys.* **10**, 021.
- Escudero, M., 2019, *J. Cosmol. Astropart. Phys.* **02**, 007.
- Escudero, M., N. Rius, and V. Sanz, 2017a, *J. High Energy Phys.* **02**, 045.
- Escudero, M., N. Rius, and V. Sanz, 2017b, *Eur. Phys. J. C* **77**, 397.
- Esmaili, A., and Y. Farzan, 2019, *J. Cosmol. Astropart. Phys.* **12**, 017.
- Farzan, Y., and E. Ma, 2012, *Phys. Rev. D* **86**, 033007.
- Farzan, Y., and S. Palomares-Ruiz, 2014, *J. Cosmol. Astropart. Phys.* **06**, 014.
- Farzan, Y., and S. Palomares-Ruiz, 2019, *Phys. Rev. D* **99**, 051702.
- Fechner, M., *et al.* (Super-Kamiokande Collaboration), 2009, *Phys. Rev. D* **79**, 112010.
- Formaggio, J. A., and G. P. Zeller, 2012, *Rev. Mod. Phys.* **84**, 1307.
- Frankiewicz, K., 2018, Ph.D. thesis (National Centre for Nuclear Research).
- Frankiewicz, K. (Super-Kamiokande Collaboration), 2015, [arXiv:1510.07999](https://arxiv.org/abs/1510.07999).
- Frankiewicz, K. (Super-Kamiokande Collaboration), 2017, *J. Phys. Conf. Ser.* **888**, 012210.
- Freedman, D. Z., 1974, *Phys. Rev. D* **9**, 1389.
- Frigerio, M., A. Pomarol, F. Riva, and A. Urbano, 2012, *J. High Energy Phys.* **07**, 015.
- Fukuda, Y., *et al.* (Super-Kamiokande Collaboration), 1998, *Phys. Rev. Lett.* **81**, 1158; **81**, 4279(E) (1998).
- Fukuda, Y., *et al.* (Super-Kamiokande Collaboration), 2003, *Nucl. Instrum. Methods Phys. Res., Sect. A* **501**, 418.
- Gainer, J. S., J. Lykken, K. T. Matchev, S. Mrenna, and M. Park, 2014, *J. High Energy Phys.* **10**, 078.
- Gandhi, R., C. Quigg, M. H. Reno, and I. Sarcevic, 1996, *Astropart. Phys.* **5**, 81.
- Gando, A., *et al.* (KamLAND Collaboration), 2012, *Astrophys. J.* **745**, 193.
- Gando, A., *et al.* (KamLAND Collaboration), 2013, *Phys. Rev. D* **88**, 033001.
- Garcia, A., R. Gauld, A. Heijboer, and J. Rojo, 2020, [arXiv:2004.04756](https://arxiv.org/abs/2004.04756).
- Glashow, S. L., 1960, *Phys. Rev.* **118**, 316.
- Glüsenkamp, T., 2018, *Eur. Phys. J. Plus* **133**, 218.
- Glüsenkamp, T., 2020, *J. Instrum.* **15**, P01035.
- Goodenough, L., and D. Hooper, 2009, [arXiv:0910.2998](https://arxiv.org/abs/0910.2998).
- Gorham, P., *et al.* (ANITA Collaboration), 2010, *Phys. Rev. D* **82**, 022004; **85**, 049901(E) (2012).
- Gorham, P., *et al.* (ANITA Collaboration), 2016, *Phys. Rev. Lett.* **117**, 071101.
- Gorham, P., *et al.* (ANITA Collaboration), 2018, *Phys. Rev. Lett.* **121**, 161102.
- Gorham, P. W., *et al.* (ANITA Collaboration), 2009, *Astropart. Phys.* **32**, 10.
- Gorham, P. W., *et al.* (ANITA Collaboration), 2019, [arXiv:1902.04005](https://arxiv.org/abs/1902.04005).
- Gozzini, S. R., 2019, *Proc. Sci. ICRC2019*, 552, <https://pos.sissa.it/358/552/pdf>.
- Griest, K., and M. Kamionkowski, 1990, *Phys. Rev. Lett.* **64**, 615.
- Gusev, G. A., and I. M. Zheleznykh, 1984, *Sov. Phys. Usp.* **27**, 550.
- Hagedorn, C., J. Herrero-García, E. Molinaro, and M. A. Schmidt, 2018, *J. High Energy Phys.* **11**, 103.
- Halzen, F., 2005, [arXiv:astro-ph/0506248](https://arxiv.org/abs/astro-ph/0506248).
- He, X.-G., G. C. Joshi, H. Lew, and R. R. Volkas, 1991a, *Phys. Rev. D* **43**, R22.
- He, X.-G., G. C. Joshi, H. Lew, and R. R. Volkas, 1991b, *Phys. Rev. D* **44**, 2118.
- Heinrich, J., and L. Lyons, 2007, *Annu. Rev. Nucl. Part. Sci.* **57**, 145.
- Heisig, J., M. Korsmeier, and M. W. Winkler, 2020, [arXiv:2005.04237](https://arxiv.org/abs/2005.04237).
- Ho, C. M., and R. J. Scherrer, 2013, *Phys. Rev. D* **87**, 023505.
- Honda, M., M. S. Athar, T. Kajita, K. Kasahara, and S. Midorikawa, 2015, *Phys. Rev. D* **92**, 023004.
- Honda, M., T. Kajita, K. Kasahara, S. Midorikawa, and T. Sanuki, 2007, *Phys. Rev. D* **75**, 043006.
- Hoof, S., A. Geringer-Sameth, and R. Trotta, 2018, [arXiv:1812.06986](https://arxiv.org/abs/1812.06986).
- Hooper, D., and L. Goodenough, 2011, *Phys. Lett. B* **697**, 412.
- Hooper, D., S. Wegsman, C. Deaconu, and A. Vieregge, 2019, *Phys. Rev. D* **100**, 043019.
- Horiuchi, S., J. F. Beacom, and E. Dwek, 2009, *Phys. Rev. D* **79**, 083013.
- Hosaka, J., *et al.* (Super-Kamiokande Collaboration), 2006, *Phys. Rev. D* **73**, 112001.
- Hostert, M., 2019, Ph.D. thesis (Durham University).
- Hou, G. W. S., 2014, [arXiv:1409.0477](https://arxiv.org/abs/1409.0477).
- Indumathi, D., 2019, in *Proceedings of the 16th Conference on Flavor Physics and CP Violation, Hyderabad, India, 2019*, edited by A. Giri and R. Mohanta (Springer International Publishing, Cham, Switzerland), pp. 309–314.
- Ishihara, A. (IceCube Collaboration), 2019, [arXiv:1908.09441](https://arxiv.org/abs/1908.09441).
- Ishihara, A., and A. Kiriki (IceCube Collaboration), 2019, [arXiv:1908.10780](https://arxiv.org/abs/1908.10780).
- Jee, M. J., *et al.*, 2007, *Astrophys. J.* **661**, 728.
- Jee, M. J., and J. A. Tyson, 2009, *Astrophys. J.* **691**, 1337.
- Jeong, Y. S., M. V. Luu, M. H. Reno, and I. Sarcevic, 2017, *Phys. Rev. D* **96**, 043003.
- Jiang, M., *et al.* (Super-Kamiokande Collaboration), 2019, *Prog. Theor. Exp. Phys.* **053F01**.
- Karukes, E. V., M. Benito, F. Iocco, R. Trotta, and A. Geringer-Sameth, 2019, [arXiv:1901.02463](https://arxiv.org/abs/1901.02463).
- Katori, T., and M. Martini, 2018, *J. Phys. G* **45**, 013001.
- Kelly, K. J., and P. A. N. Machado, 2018, *J. Cosmol. Astropart. Phys.* **10**, 048.
- Khatun, A., R. Laha, and S. K. Agarwalla, 2017, *J. High Energy Phys.* **06**, 057.
- Klop, N., and S. Ando, 2018, *Phys. Rev. D* **98**, 103004.
- Kolb, E. W., M. S. Turner, and T. P. Walker, 1986, *Phys. Rev. D* **34**, 2197.
- Kurylov, A., M. Ramsey-Musolf, and P. Vogel, 2003, *Phys. Rev. C* **67**, 035502.
- Laha, R., and J. F. Beacom, 2014, *Phys. Rev. D* **89**, 063007.
- Leane, R. K., and T. R. Slatyer, 2019, *Phys. Rev. Lett.* **123**, 241101.
- Learned, J. G., and S. Pakvasa, 1995, *Astropart. Phys.* **3**, 267.
- Lees, J. P., *et al.* (BABAR Collaboration), 2014, *Phys. Rev. Lett.* **113**, 201801.

- Leo, W., 1994, *Techniques for Nuclear and Particle Physics Experiments: A How-To Approach* (Springer, New York).
- Li, S. W., and J. F. Beacom, 2014, *Phys. Rev. C* **89**, 045801.
- Linyan, W., 2018, Ph.D. Thesis (Tsinghua University).
- Liu, Q., J. Lazar, C. A. Argüelles, and A. Kheirandish, 2020, *J. Cosmol. Astropart. Phys.* **10**, 043.
- Loewy, A., S. Nussinov, and S. L. Glashow, 2014, [arXiv:1407.4415](https://arxiv.org/abs/1407.4415).
- Lopez-Honorez, L., O. Mena, S. Palomares-Ruiz, and A. C. Vincent, 2013, *J. Cosmol. Astropart. Phys.* **07**, 046.
- Lu, L., 2019, Proc. Sci. ICRC2019, 945, <https://pos.sissa.it/358/945/pdf>.
- Markov, M., and I. Zheleznykh, 1986, *Nucl. Instrum. Methods Phys. Res., Sect. A* **248**, 242.
- McKeen, D., and N. Raj, 2018, [arXiv:1812.05102](https://arxiv.org/abs/1812.05102).
- MicroBooNE Collaboration, 2018, technical report, <https://doi.org/10.2172/1573220>.
- Migenda, J. (Hyper-Kamiokande Proto Collaboration), 2017, Proc. Sci. EPS-HEP2017, 020 [[arXiv:1710.08345](https://arxiv.org/abs/1710.08345)].
- Muñoz, J. B., and A. Loeb, 2018, *Nature (London)* **557**, 684.
- Murase, K., and J. F. Beacom, 2012, *J. Cosmol. Astropart. Phys.* **10**, 043.
- Murase, K., D. Guetta, and M. Ahlers, 2016, *Phys. Rev. Lett.* **116**, 071101.
- Murase, K., R. Laha, S. Ando, and M. Ahlers, 2015, *Phys. Rev. Lett.* **115**, 071301.
- Murase, K., and I. M. Shoemaker, 2019, *Phys. Rev. Lett.* **123**, 241102.
- Nagai, R., and A. Ishihara (IceCube Collaboration), 2019, [arXiv:1908.11564](https://arxiv.org/abs/1908.11564).
- Nollett, K. M., and G. Steigman, 2014, *Phys. Rev. D* **89**, 083508.
- Nollett, K. M., and G. Steigman, 2015, *Phys. Rev. D* **91**, 083505.
- Olinto, A. V., *et al.*, 2020, [arXiv:2012.07945](https://arxiv.org/abs/2012.07945).
- Olivares-Del Campo, A., 2019, Ph.D. thesis (Durham University).
- Olivares-Del Campo, A., C. Boehm, S. Palomares-Ruiz, and S. Pascoli, 2018, *Phys. Rev. D* **97**, 075039.
- Olivares-Del Campo, A., S. Palomares-Ruiz, and S. Pascoli, 2018, [arXiv:1805.09830](https://arxiv.org/abs/1805.09830).
- Palomares-Ruiz, S., and S. Pascoli, 2008, *Phys. Rev. D* **77**, 025025.
- Pandey, S., S. Karmakar, and S. Rakshit, 2019, *J. High Energy Phys.* **01**, 095.
- Patel, H. H., S. Profumo, and B. Shakya, 2019, [arXiv:1912.05581](https://arxiv.org/abs/1912.05581).
- Pato, M., F. Iocco, and G. Bertone, 2015, *J. Cosmol. Astropart. Phys.* **12**, 001.
- Persic, M., P. Salucci, and F. Stel, 1996, *Mon. Not. R. Astron. Soc.* **281**, 27.
- Prada, F., A. A. Klypin, A. J. Cuesta, J. E. Betancort-Rijo, and J. Primack, 2012, *Mon. Not. R. Astron. Soc.* **423**, 3018.
- Press, W. H., and P. Schechter, 1974, *Astrophys. J.* **187**, 425.
- Primulando, R., and P. Uttayarat, 2018, *J. High Energy Phys.* **06**, 026.
- Profumo, S., F. S. Queiroz, J. Silk, and C. Siqueira, 2018, *J. Cosmol. Astropart. Phys.* **03**, 010.
- Psihas, F., E. Niner, M. Groh, R. Murphy, A. Aurisano, A. Himmel, K. Lang, M. Messier, A. Radovic, and A. Sousa, 2019, *Phys. Rev. D* **100**, 073005.
- Queiroz, F. S., C. E. Yaguna, and C. Weniger, 2016, *J. Cosmol. Astropart. Phys.* **05**, 050.
- Reno, M. H., J. F. Krizmanic, and T. M. Venters, 2019, *Phys. Rev. D* **100**, 063010.
- Reno, M. H., T. M. Venters, J. F. Krizmanic, L. A. Anchordoqui, C. Guepin, and A. V. Olinto (POEMMA Collaboration), 2020, Proc. Sci. ICRC2019, 989 [[arXiv:1908.03603](https://arxiv.org/abs/1908.03603)].
- Richard, E., *et al.* (Super-Kamiokande Collaboration), 2016, *Phys. Rev. D* **94**, 052001.
- Romero-Wolf, A., *et al.*, 2019, *Phys. Rev. D* **99**, 063011.
- Romero-Wolf, A., *et al.*, 2020, [arXiv:2002.06475](https://arxiv.org/abs/2002.06475).
- Rubin, V. C., J. Ford, and W. Kent, 1970, *Astrophys. J.* **159**, 379.
- Sabti, N., J. Alvey, M. Escudero, M. Fairbairn, and D. Blas, 2020, *J. Cosmol. Astropart. Phys.* **01**, 004.
- Safa, I., A. Pizzuto, C. A. Argüelles, F. Halzen, R. Hussain, A. Kheirandish, and J. Vandenbroucke, 2019, [arXiv:1909.10487](https://arxiv.org/abs/1909.10487).
- Sasaki, M., 2019, Proc. Sci. ICRC, 1003, <https://pos.sissa.it/358/1003/pdf>.
- Sasaki, M. (NTA Collaboration), 2018, Proc. Sci. ICRC2017, 941.
- Schneider, A., 2019, [arXiv:1907.11266](https://arxiv.org/abs/1907.11266).
- Seckel, D., 1998, *Phys. Rev. Lett.* **80**, 900.
- Serpico, P. D., and G. G. Raffelt, 2004, *Phys. Rev. D* **70**, 043526.
- Sheth, R. K., H. J. Mo, and G. Tormen, 2001, *Mon. Not. R. Astron. Soc.* **323**, 1.
- Sheth, R. K., and G. Tormen, 1999, *Mon. Not. R. Astron. Soc.* **308**, 119.
- Shoemaker, I. M., 2013, *Phys. Dark Universe* **2**, 157.
- Shoemaker, I. M., A. Kusenko, P. K. Munneke, A. Romero-Wolf, D. M. Schroeder, and M. J. Siegart, 2019, [arXiv:1905.02846](https://arxiv.org/abs/1905.02846).
- Sjöstrand, T., 2020, *Comput. Phys. Commun.* **246**, 106910.
- Sjöstrand, T., S. Ask, J. R. Christiansen, R. Corke, N. Desai, P. Ilten, S. Mrenna, S. Prestel, C. O. Rasmussen, and P. Z. Skands, 2015, *Comput. Phys. Commun.* **191**, 159.
- Smirnov, J., and J. F. Beacom, 2019, *Phys. Rev. D* **100**, 043029.
- Smith, S., 1936, *Astrophys. J.* **83**, 23.
- Sousa, A., 2007, Fermilab Report No. FERMILAB-CONF-07-176-E.
- Sousa, A. B. (MINOS and MINOS+ Collaborations), 2015, *AIP Conf. Proc.* **1666**, 110004.
- Stachurska, J., 2018, <https://doi.org/10.5281/zenodo.1301122>.
- Stachurska, J. (IceCube Collaboration), 2020, Proc. Sci. ICRC2019, 1015 [[arXiv:1908.05506](https://arxiv.org/abs/1908.05506)].
- Steigman, G., 2013, *Phys. Rev. D* **87**, 103517.
- Steigman, G., B. Dasgupta, and J. F. Beacom, 2012, *Phys. Rev. D* **86**, 023506.
- Steigman, G., and K. M. Nollett, 2014, *Mem. Soc. Astron. Ital.* **85**, 175 [[arXiv:1401.5488v1](https://arxiv.org/abs/1401.5488v1)].
- Sui, Y., and P. S. Bhupal Dev, 2018, *J. Cosmol. Astropart. Phys.* **07**, 020.
- Tanabashi, M., *et al.* (Particle Data Group), 2018, *Phys. Rev. D* **98**, 030001.
- Tinker, J. L., A. V. Kravtsov, A. Klypin, K. Abazajian, M. S. Warren, G. Yepes, S. Gottlober, and D. E. Holz, 2008, *Astrophys. J.* **688**, 709.
- Trotta, R., 2017, [arXiv:1701.01467](https://arxiv.org/abs/1701.01467).
- Vogel, P., and J. F. Beacom, 1999, *Phys. Rev. D* **60**, 053003.
- Watanabe, H., H. Zhang, K. Abe, Y. Hayato, T. Iida, M. Ikeda, J. Kameda, K. Kobayashi, Y. Koshio, and M. Miura (Super-Kamiokande Collaboration), 2009, *Astropart. Phys.* **31**, 320.
- Watson, W. A., I. T. Iliev, A. D'Aloisio, A. Knebe, P. R. Shapiro, and G. Yepes, 2013, *Mon. Not. R. Astron. Soc.* **433**, 1230.
- Wilkinson, R. J., A. C. Vincent, C. Boehm, and C. McCabe, 2016, *Phys. Rev. D* **94**, 103525.
- Wissel, S., J. Alvarez-Muñiz, W. R. Carvalho, A. Romero-Wolf, H. Schoorlemmer, and E. Zas, 2019, *EPJ Web Conf.* **216**, 04007.
- Wissel, S., *et al.*, 2020, [arXiv:2004.12718](https://arxiv.org/abs/2004.12718).
- Yüksel, H., S. Horiuchi, J. F. Beacom, and S. Ando, 2007, *Phys. Rev. D* **76**, 123506.
- Zas, E., F. Halzen, and T. Stanev, 1992, *Phys. Rev. D* **45**, 362.
- Zas, E. (Pierre Auger Collaboration), 2018, Proc. Sci. ICRC2017, 972.
- Zhou, B., and J. F. Beacom, 2020a, *Phys. Rev. D* **101**, 036010.
- Zhou, B., and J. F. Beacom, 2020b, *Phys. Rev. D* **101**, 036011.
- Zwicky, F., 1937, *Astrophys. J.* **86**, 217.